Nanoscale Advances

ROYAL SOCIETY OF CHEMISTRY

PAPER

View Article Online
View Journal | View Issue

Cite this: *Nanoscale Adv.*, 2025, **7**, 3485

Designing a Z-scheme rGO–SnS_2 synergistic photocatalyst for photocatalytic mineralization of atrazine and 2,4-dichlorophenoxyacetic acid and applying machine learning for predictive modelling of photocatalytic performance†

Jinal Patel,[a] Megha Parmar,[a] Syed Shahabuddin,*[a] Inderjeet Tyagi,[b] Suhas [c] and Rama Gaur *[a]

The extensive use of agrochemicals for crop protection and quality enhancement has raised environmental concerns due to their negative effects on human health. This study focuses on the design and synthesis of a Z-scheme rGO–SnS_2 photocatalyst for wastewater treatment. rGO–SnS_2 nanocomposites with varying SnS_2 nanoparticle loadings were synthesized using a thermal decomposition method and characterized using various analytical techniques to confirm their composition, phase, structure, morphology, optical properties, and functional groups. The photocatalytic performance of the rGO–SnS_2 nanocomposites was evaluated for the degradation of atrazine (ATZ) and 2,4-dichlorophenoxyacetic acid (2,4-D) in aqueous solutions under natural sunlight. The optimized nanocomposite achieved fast and efficient degradation, with a removal efficiency of 91% for ATZ and 87% for 2,4-D within 3 minutes, compared to only 18% and 26% removal by pure rGO. The study also explored key parameters affecting photocatalytic performance, including catalyst loading, pH, dosage, and regeneration. The degradation pathways and major intermediates of ATZ and 2,4-D were identified using LC-MS analysis, and a detailed reaction mechanism was proposed based on scavenger and mineralization studies. Additionally, machine learning (ML) models, including Gaussian process (GP), artificial neural network (ANN), and support vector machine (SVM), were employed exclusively for predictive analysis of the photocatalytic performance. ANN demonstrated the best predictive capability, with an R^2 value of 0.974 and an error of 0.002. This work highlights the potential of rGO–SnS_2 nanocomposites as effective photocatalysts for agrochemical mineralization, with ML aiding in performance prediction for real-world applications.

Received 12th February 2025
Accepted 15th April 2025

DOI: 10.1039/d5na00143a

rsc.li/nanoscale-advances

1. Introduction

To meet the growing demand for food, the agricultural industry has significantly expanded its use of agrochemicals and pesticides. The accumulation of these agrochemical residues in water bodies threatens marine life and overall ecosystem health. This has raised concerns about their environmental impact, particularly on water quality and aquatic biodiversity. Water pollution has become a critical environmental issue, affecting water bodies worldwide. Agrochemicals have been detected in surface water, groundwater, and drinking water sources, posing significant threats to ecosystems and human health. Their use presents considerable environmental and health challenges. Exposure to agrochemicals can occur through direct contact, consumption of contaminated water and food, and inhalation. Additionally, agrochemicals can leach into groundwater, discharge into surface water bodies, and persist in the soil.[1]

This study focuses on atrazine and 2,4-dichlorophenoxyacetic acid (2,4-D), two of the oldest and most extensively used agrochemicals due to their effectiveness and relatively low cost in agriculture. Atrazine is an herbicide primarily used to control broadleaf and grassy weeds.[2] It belongs to the triazine class of herbicides and has been extensively utilized in agriculture, forestry, aquatic systems, and residential areas.[3] It is soluble in water, facilitating its presence in groundwater and surface water. 2,4-Dichlorophenoxyacetic acid (2,4-D) is a widely used herbicide for controlling broadleaf weeds in cereal crops like

[a]Department of Chemistry, School of Energy Technology, Pandit Deendayal Energy University, Gandhinagar 382426, Gujarat, India. E-mail: rama.gaur@sot.pdpu.ac.in; syed.shahabuddin@sot.pdpu.ac.in

[b]Centre for DNA Taxonomy, Molecular Systematics Division, Zoological Survey of India, Ministry of Environment, Forests and Climate Change, Kolkata 700053, West Bengal, India

[c]Department of Chemistry, Gurukul Kangri (Deemed to be University), Hardwar 249404, Uttarakhand, India

† Electronic supplementary information (ESI) available. See DOI: https://doi.org/10.1039/d5na00143a

wheat, corn, and rice, and managing fast-growing plants that can disrupt ecosystems.[4] It belongs to the phenoxy family of herbicides.[5] Despite their extensive use, these agrochemicals are associated with various health and environmental risks.[6] The literature indicates that health risks include acute poisoning, endocrine disruption, decreased fertility, birth defects, cancer, and neurological disorders. Although these agrochemicals do not persist as long as some other herbicides, their residues can still impact soil and water for extended periods, posing long-term environmental risks.[4] During the degradation process, reactive species can attack the molecules of these agrochemicals, breaking chemical bonds and leading to the formation of secondary pollutants. Sometimes, these secondary pollutants can be more toxic than the original compounds, making the removal of these metabolites crucial for improving water quality and maintaining a healthy environment.

Several methods are commonly employed for wastewater treatment, including adsorption, membrane filtration, ion exchange, and photocatalysis, each serving different purposes.[7–11] Among these, photocatalysis offers promising properties that make it particularly appealing for environmental remediation and sustainable processes.[12,13] It is favored by researchers for its ability to activate photocatalysts, generate reactive species, degrade contaminants, and disinfect water using light energy.[14] In the last decade, advanced oxidation processes (AOPs) and heterogeneous photocatalysis have developed as effective alternatives for wastewater treatment using photocatalysts.

In recent years, researchers have increasingly focused on graphene and its derivatives due to their special properties, including high surface area, good physicochemical stability, electron mobility, high adsorption capacity, and ease of fabrication *via* chemical reduction methods.[15] The effectiveness of photocatalytic processes involving a catalyst is significantly affected by its electronic structure and the energy of its band gap.[10] For an efficient photocatalyst, reduced graphene oxide (rGO) has a smaller band gap than graphene oxide (GO), extending light absorption into the visible region. However, pure rGO suffers from lower photocatalytic efficiency due to higher recombination rates of charge carriers generated by light. This issue can be addressed by combining rGO with other materials to form binary nanocomposites.

Researchers have already reported various rGO-based heterojunctions, such as B-rGO/$PbTiO_3$,[16] rGO-ZnO/WO_3,[17] Cu_2O/rGO/$BiVO_4$,[18] and $AgZrO_2$/rGO,[19] for diverse applications. Recently, the development of Z-scheme photocatalytic systems has emerged as a promising strategy to increase interfacial charge transfer and improve the separation of photogenerated electron–hole pairs while maintaining superior redox capabilities. Although many semiconductor materials have unique optical properties, some have limitations. SnS_2, with its photochemical properties, electronic band structure, high carrier mobility, stability, and a narrow band gap (2.5 eV), has proven useful in various applications.[20] SnS_2 also has suitable band edges that can align well with those of rGO, potentially forming an effective Z-scheme photocatalytic system.[21] To date, there are only a few reports on the preparation of binary and ternary nanocomposites using rGO and SnS_2, such as rGO/SnS_2, rGO/SnS_2/Fe_3O_4, rGO/SnS_2/Ag, and rGO/SnS_2/g-C_3N_4, specifically for photocatalytic degradation of contaminants.[22–25] Machine learning (ML) models are widely used in various sectors, such as healthcare, finance, e-commerce, pharmaceutical industry, *etc.*, for predictive analysis, giving valuable insights, optimization of the process, and acceleration of the decision-making process.[26] Various models, artificial neural networks, Gaussian processes, support vector machines, Gaussian processes, and decision trees are available to train and test the data sets. Ignacio Melendez-Pastor Co *et al.* utilized machine learning for the determination of influencing environmental factors responsible for the accumulation of DDT-DDE in the watercourses. Their study revealed how machine learning could be used to determine the spatial distributions in agricultural drainage systems.[27] Kyung Hwa Cho Co *et al.* simulated the photocatalytic degradation of a toxic dye using NM–Bi–Fe–O_3 and the CatBoost model. Their findings revealed that reaction conditions are more important than the photocatalyst properties, and the model simulated the dye degradation with a root mean square error of 1.34.[28]

This study reports the successful synthesis of a Z-scheme rGO–SnS_2 photocatalyst using a one-pot thermal decomposition approach and its application in the photocatalytic degradation of ATZ and 2,4-D from aqueous solutions. A comprehensive degradation mechanism has been proposed based on experimental results from pH studies, scavenger experiments, and LC-MS investigations, providing insight into the degradation pathways and intermediates of these agrochemicals. The synthesized rGO–SnS_2 nanocomposites demonstrate high efficiency for environmental remediation. Additionally, robust machine learning (ML) methodologies, including artificial neural networks (ANN), Gaussian process (GP), and support vector machines (SVM), were employed to predict the removal efficiency of the nanocomposite. While the primary focus of this work is the synthesis and application of the Z-scheme rGO–SnS_2 photocatalyst, ML was incorporated as a secondary tool for predictive analysis. By integrating experimental results with ML algorithms, this study enhances the adaptability of the nanocomposite for real-world applications, providing a deeper understanding of the key parameters influencing photocatalytic performance and enabling targeted optimization for improved efficiency.

2. Materials

All the chemicals used for the synthesis of reduced graphene oxide (rGO) and conducting photocatalytic studies were as follows: graphite powder (HPLC grade), graphene oxide (GO, synthesized by Hummer's method), ammonia solution (Finar), ethanol, chloroform (Merck), ascorbic acid (Merck), hydrogen peroxide (H_2O_2, Merck 30%), thiourea (SRL 99% purity), tin(IV) chloride (Sigma-Aldrich, 98% purity), diphenyl ether(Sigma-Aldrich 99% purity), commercial atrazine (Traxx, 50% purity), 2,4-dichlorophenoxyacetic acid (2,4-D, Sigma-Aldrich, 95% purity), ammonium oxalate monohydrate (Finar), isopropanol

(Finar, 99% purity), *p*-benzoquinone (Sigma-Aldrich, 98%), silver nitrate (ACS grade), and methanol (Finar Chemicals, India). All chemicals were used as received. Distilled water was used for all synthesis and photocatalytic experiments.

2.1. Synthesis of graphene oxide (GO)

GO was synthesized using a modified Hummers' method.[29] For the preparation of GO, a mixture of 1 g of graphite, 1 g of sodium nitrate ($NaNO_3$), and 50 ml of sulfuric acid (H_2SO_4) was placed in a beaker and stirred in an ice bath for 15 minutes, maintaining the temperature below 10 °C. After 15 minutes, 3 g of potassium permanganate ($KMnO_4$) powder was added to the solution slowly, with continuous stirring for 30 minutes, under a temperature below 20 °C. The mixture was then heated at 35 °C for 30 minutes. Distilled water was added to the mixture, and the temperature was raised and maintained at 90 °C. After 30 minutes, additional distilled water and 30% hydrogen peroxide (H_2O_2) were added to the beaker to stop the reaction. The product was washed using a 5% hydrochloric acid (HCl) solution and distilled water until a neutral pH (pH = 7) was achieved. Finally, the product GO was kept in an oven to dry at 80 °C for 24 hours. Scheme 1(a) illustrates the steps involved in preparing graphene oxide.

2.2. Synthesis of reduced graphene oxide (rGO)

rGO was prepared using the chemical reduction method.[30] For the synthesis of rGO, ascorbic acid was used as the reducing agent. First, 400 mg of GO was added to a beaker and dissolved in distilled water. Once the GO was fully suspended, 4 grams of ascorbic acid were added to the beaker, and the mixture was stirred for 30 minutes at 60 °C. After the reaction, the solution was centrifuged to achieve complete separation. Next, 30% hydrogen peroxide (H_2O_2) was added to the solution to oxidize any excess ascorbic acid, and the mixture was stirred for an additional 30 minutes at 60 °C. After this step, the solution was centrifuged again to separate the product. The rGO was washed with ethanol, followed by distilled water, until a neutral pH (pH = 7) was achieved. The rGO sample was then dried in an oven at 120 °C for 24 h. Scheme 1(b) illustrates the steps involved in preparing reduced graphene oxide.

2.3. Synthesis of SnS_2 nanoparticles

A simple, one-pot thermal decomposition method was used to synthesize SnS_2 nanoparticles.[31] Tin chloride (1 mM), thiourea (2 mM), and diphenyl ether (10 ml) were added to a round-bottom flask. The reaction mixture was then refluxed at 180 °C for 1 hour. A change in the color of the mixture to dark yellow indicated the formation of SnS_2 nanoparticles. After the reaction, the mixture was cooled to room temperature and precipitated with excess methanol. The precipitate was centrifuged and washed with methanol. Finally, the product was dried overnight in an oven at 80 °C.

2.4. Synthesis of rGO–SnS_2 nanocomposites

The rGO–SnS_2 nanocomposites were synthesized using a thermal decomposition method, with varying loadings of SnS_2 (0.125 mM, 0.25 mM, 0.5 mM, and 1 mM). To prepare the nanocomposites, 100 mg of rGO, tin chloride, and thiourea in 10 ml of diphenyl ether were added to a round-bottom flask. The same procedure described in Section 2.4 was followed for the synthesis. The details and nomenclature of the nanocomposites prepared in this study are summarized in Table 1. Scheme 1(c) illustrates the schematic representation of the preparation of rGO–SnS_2 nanocomposites.

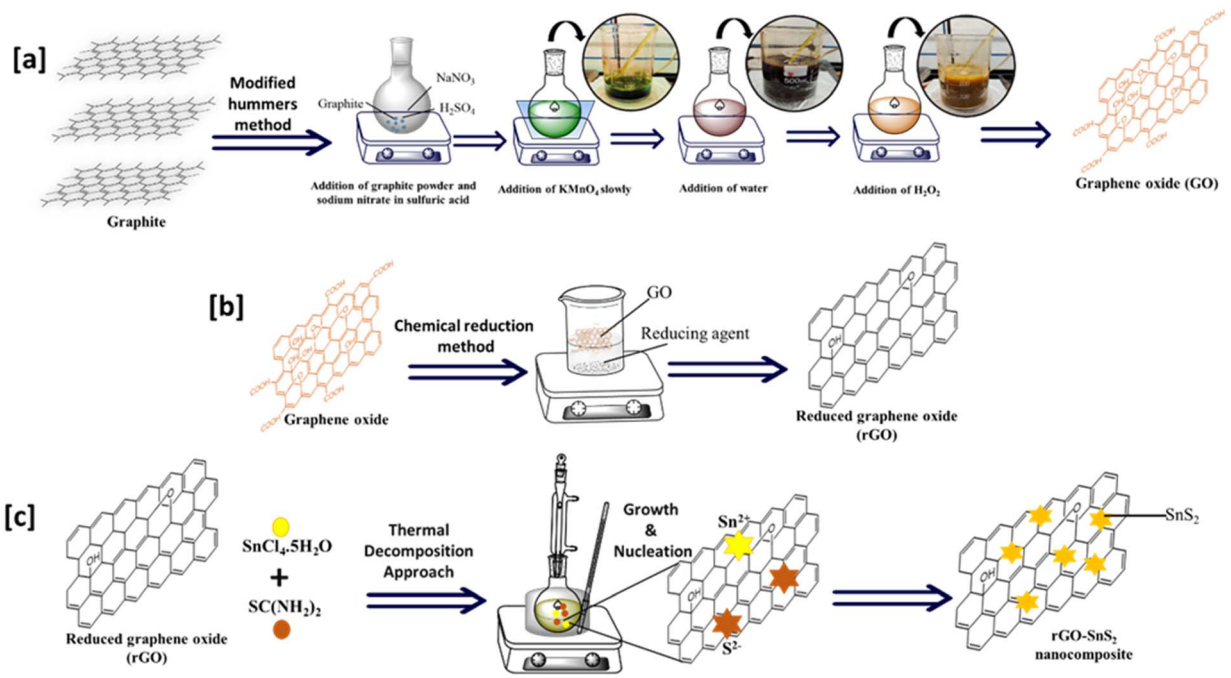

Scheme 1 Schematic representation of the preparation of (a) GO, (b) rGO, and (c) rGO–SnS_2 nanocomposites.

Table 1 Synthetic details and nomenclature of rGO–SnS_2 samples prepared *via* the thermal decomposition approach

Code	rGO	Temp. and time	Tin chloride used	Thiourea used
SnS_2	—	180 °C, 1 h	1 mmol	2 mmol
rGO	—	—	—	—
RS-0.125	100 mg	180 °C, 1 h	0.125 mmol	0.25 mmol
RS-0.25	100 mg	180 °C, 1 h	0.25 mmol	0.5 mmol
RS-0.5	100 mg	180 °C, 1 h	0.5 mmol	1 mmol
RS-1	100 mg	180 °C, 1 h	1 mmol	2 mmol

2.5. Characterization

The rGO–SnS_2 nanocomposites were characterized using various analytical techniques to evaluate their phase, structure, optical properties, functional groups, thermal stability, and morphology. Phase analysis was conducted using powder X-ray diffraction, with patterns recorded on a Rigaku MiniFlex 600 C diffractometer employing filtered Cu Kα radiation ($\lambda = 1.53$ Å) over a 2θ range of 20 to 80°, with a scan speed of 4° per minute. Raman spectral analysis was performed using a Horiba LabRam HR spectrometer over 300 to 3000 cm^{-1}. Diffuse Reflectance Spectroscopy (DRS) spectra were obtained using a PerkinElmer Lambda 365+ UV-Vis spectrophotometer in the 200 to 800 nm range. Fourier Transform Infrared (FT-IR) analysis was performed using a PerkinElmer Spectrum instrument in the 4000 to 500 cm^{-1} range in Attenuated Total Reflectance (ATR) mode. Thermal analysis was performed with a HITACHI STA7200 thermogravimetric analyzer. The heating rate was set to 10 °C min^{-1} under airflow (99.99%) or nitrogen (99.99%) at a flow rate of 20 ml min^{-1}, and the temperature was raised to 750 °C. The morphology of the nanocomposites was analyzed using a ZEISS Ultra 55 field emission scanning electron microscope (FE-SEM). The aluminum substrate was cleaned with isopropanol, and the sample was mounted on carbon tape on an aluminum stub and then coated with a thin layer of gold for 30 seconds under vacuum to make the sample conductive. Transmission electron microscopy (TEM) images were obtained using a JEOL TEM operating at an accelerating voltage of 180 kV. For TEM measurements, a few drops of sample suspension in methanol were placed on carbon-coated copper grids and allowed to dry in the air. UV-visible spectra for photocatalytic degradation studies were recorded using a LABINDIA UV-visible spectrometer in the 200 to 800 nm range. Mott–Schottky (M-S) analysis was done using a three-electrode system with a glassy carbon electrode (GCE) as the working electrode, a platinum wire as the counter electrode, and sodium sulphate as the electrolyte (more details are given in the ESI†).

2.6. Photocatalytic studies

The photocatalytic activities of rGO, SnS_2, and rGO–SnS_2 (RS) nanocomposites were monitored using UV-visible spectroscopy. For the photocatalytic degradation experiments, 1 mg ml^{-1} of each photocatalyst was added to aqueous solutions of atrazine (ATZ, 10 ppm) and 2,4-dichlorophenoxyacetic acid (2,4-D, 10 ppm), in a test tube, and the solutions were sonicated to ensure uniform dispersion. After dispersion, the samples were exposed to natural sunlight for 3 minutes. Following irradiation, the slurries were centrifuged, and the supernatant solutions were analyzed using a UV-Vis spectrophotometer. The degradation of ATZ and 2,4-D was monitored by observing the characteristic absorption peaks at 220 nm and 200 nm, respectively. The photocatalytic mineralization of agrochemicals in aqueous solutions using rGO–SnS_2 as the photocatalyst was conducted at Pandit Deendayal Energy University, Gandhinagar, Gujarat, India. The experiments took place during the month of April 2024, from 12:00 to 3:00 PM. The exact location coordinates are: latitude: 23.2156° N, longitude: 72.6369° E (**https://www.suncalc.org/#/21.5074,73.9412,5/2025.03.29/11:27/1/3**).

Parameter studies, including loading, dosage, pH, and regenerability, were conducted to determine the optimal conditions for the photocatalytic degradation of agrochemicals.

The loading study aimed to evaluate the effect of varying SnS_2 nanoparticle loading on the photocatalytic performance of the nanocomposites. Degradation studies were performed with different photocatalyst dosages (0.1, 0.25, 0.5, 1, and 2 mg ml^{-1}) to assess their impact on the degradation of both agrochemicals. The effect of pH on degradation was examined by preparing agrochemical solutions at various pH levels, ranging from 2 to 12, using 1 M HCl and 1 M NaOH solutions.

To assess the photochemical stability of the materials and their potential for reuse, a regenerability study was conducted. This involved measuring the photocatalysts' X-ray diffraction (XRD) patterns before and after degradation. A scavenger study was performed to identify the active species involved in the degradation process. The study was conducted in the presence and absence of various scavengers. Different scavengers, such as ammonium oxalate (AO, 1 mmol), silver nitrate ($AgNO_3$, 1 mmol), benzoquinone (BQ, 0.1 mmol), and isopropanol (IPA, 1 mmol), were used to target holes, electrons, superoxide radicals, and hydroxyl radicals, respectively. Scavengers were added to the agrochemical solutions, followed by the addition of the photocatalyst (1 mg ml^{-1}). The mixture was exposed to natural sunlight for 3 minutes and then sampled and analyzed using a UV-visible spectrometer.

2.7. LC-MS analysis

After the photodegradation studies, an LC-MS analysis was carried out to investigate the degradation pathways of the photodegraded product. For the LC-MS analysis, both blank and post-degradation solutions of ATZ and 2,4-D were examined to identify degradation products. The 2,4-D solution was prepared using acetonitrile (HPLC grade) (acetonitrile : H_2O ratio: 4 : 6). The ATZ solution was prepared using methanol (methanol : H_2O ratio: 7.5 : 2.5). These solutions were analyses using a liquid chromatography-mass spectroscopy (LC-MS) (Agilent) instrument (Bio Q-TOF, MS type-QTOF).

3. Results and discussion

3.1. XRD analysis

The XRD patterns of rGO, SnS_2, and RS nanocomposites are shown in Fig. 1a. The XRD pattern of rGO exhibits a strong

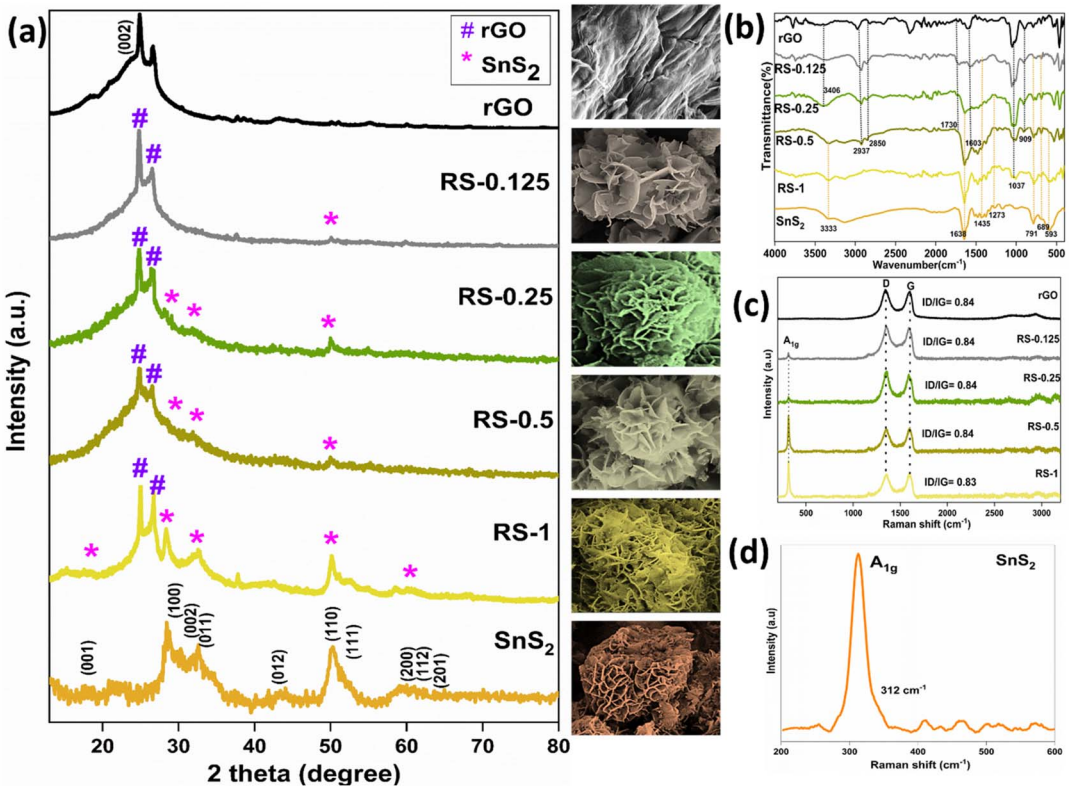

Fig. 1 (a) XRD pattern, (b) FT-IR spectra of rGO, SnS_2, and RS nanocomposites and Raman spectra of (c) rGO, RS nanocomposites, and (d) SnS_2 nanoparticles.

reflection at a 2θ value of 24.9°, corresponding to the (002) plane.[32] It indicates the presence of graphitic carbon with an interlayer spacing of 3.37 nm. The XRD pattern of SnS_2, which matches the JCPDS file no. 83-1705, confirms its hexagonal structure.[33] The SnS_2 XRD peaks at 2θ values of 15.08°, 28.29°, 30.40°, 32.18°, 42.02°, 50.13°, and 52.6° are indexed to (001), (100), (002), (011), (012), (110), and (111) reflections, respectively.

In the RS nanocomposites, characteristic peaks of both materials are observed at 2θ values of 26.48°, 28.29°, 32.18°, and 50.13°, corresponding to the (002), (100), (011), and (110) planes, confirming the formation of the nanocomposites. The *d*-spacing and average crystallite size of rGO, SnS_2, and RS nanocomposites were calculated using reflections at 24.9° and 50.13° with Bragg's and Scherrer's equations. The obtained values are provided in Table 2.

Table 2 Crystallite size and D spacing values of rGO, SnS_2, and RS nanocomposites

	rGO ($2\theta = 24.9°$)		SnS_2 ($2\theta = 50.13°$)	
Samples	Crystallite size (nm)	D spacing (Å)	Crystallite size (nm)	D spacing (Å)
rGO	20.093	3.573	—	—
RS-1	30.518	3.573	11.953	1.816
RS-0.5	17.957	3.587	10.530	1.819
RS-0.25	20.454	3.587	9.666	1.817
RS-0.125	23.140	3.587	6.093	1.812
SnS_2	—	—	3.616	1.804

3.2. FT-IR analysis

The FT-IR spectra of rGO, SnS_2, and RS nanocomposites are shown in Fig. 1b. In the rGO spectrum, the peak at 1037 cm^{-1} is attributed to the C–O stretching vibrations of the C–O–C group. The peak at 1603 cm^{-1} indicates the C=C stretch from the oxidized graphitic domain 25. The peak at 1730 cm^{-1} corresponds to the C=O stretch of the carboxyl group. Peaks at 2850 cm^{-1} and 2937 cm^{-1} are attributed to C–H symmetric and asymmetric CH_2 stretching, respectively. The broad peak at 3406 cm^{-1} is due to O–H stretching from hydroxyl groups.[10]

In the SnS_2 IR spectrum, the peaks at 593 cm^{-1} and 791 cm^{-1} are attributed to the bending and stretching vibrations of the C–S group. The peak at 689 cm^{-1} corresponds to the Sn–S bond formation.[23] The peak at 1273 cm^{-1} is associated with C–OH stretching vibrations. The peak at 1435 cm^{-1} is related to C–H bending vibrations. The peaks around 1638 cm^{-1} and 3333 cm^{-1} are ascribed to hydroxyl groups' stretching and bending vibrations.

In the RS nanocomposites, the characteristic peaks of rGO and SnS_2 are observed at 1603 cm^{-1} and 689 cm^{-1}, corresponding to the C=C stretching and Sn–S stretching, respectively. The IR spectrum of the RS nanocomposites confirms the presence of both rGO and SnS_2, indicating the successful formation of the nanocomposites.

3.3. Raman analysis

Raman spectroscopy confirms the presence of carbon disorder and defects in the prepared samples, as shown in Fig. 1c and d. The rGO spectrum exhibits two strong Raman bands: the D band at 1341 cm^{-1} and the G band at 1593 cm^{-1}.[34] Additionally, the 2D band appears at 2730 cm^{-1}. These bands indicate the presence of ring and chain structures, reflecting the multilayer nature of the graphene. In rGO, the I_D/I_G ratio decreased due to the conversion of sp^3 to sp^2 carbon atoms.[35] The G band intensity is lower than that of the D band due to the increased number of sp^2 carbon atoms, with the G band shifted to a lower wavenumber. The D/G intensity ratio confirms the existence of more defects and disorder in the structure, with rGO showing an I_D/I_G ratio of 0.84 due to the sp^2 domains formed during the reduction process.[36]

The SnS_2 spectrum features an intense peak at 312 cm^{-1}, assigned to the A1g mode of SnS_2 (as shown in Fig. 1d). The Raman spectra confirm the formation of SnS_2 nanoparticles in the 2H polytype.[31] However, the intensity of the A1g mode was reduced with a decrease in the loading of SnS_2 in the nanocomposites. In the RS nanocomposites, the characteristic peaks of SnS_2 at 312 cm^{-1} and the D (1341 cm^{-1}) and G (1593 cm^{-1}) bands of rGO are observed. The Raman spectral results indicate the successful formation of the nanocomposites.

3.4. TGA analysis

Fig. 2 shows the thermogravimetric curves of rGO, SnS_2, and RS-1 nanocomposites. All samples exhibit three main stages of weight loss in the TGA curves. For the rGO, the DTG analysis shows peaks at 50 °C (adsorbed water release), 207 °C (degradation of oxygen-containing groups in rGO), and 320 °C (decomposition of stable groups or impurities), indicating a transition to a more thermally stable carbon structure. The rGO sample shows high thermal stability after oxygen group removal, with clear weight loss stages corresponding to moisture, functional group, and impurity removal, confirming efficient reduction and stability above 320 °C. For the SnS_2, the DTG analysis shows peaks at 50 °C (adsorbed water release) and 328 °C (removal of chemically bonded water and partial decomposition of SnS_2), and thermal decomposition of SnS_2 due to sulfur release or structural changes. Weight loss up to 50 °C is due to moisture, while decomposition at higher temperatures relates to sulfur loss or transformation into a stable tin-based compound. SnS_2 remains thermally stable up to 328 °C, making it suitable. The TGA/DTG analysis of the RS-1 nanocomposite shows weight loss below 150 °C (moisture evaporation), a peak at ~264 °C (removal of oxygen groups from rGO), and a peak at ~396 °C (thermal decomposition of SnS_2, possibly sulfur release). The peak at ~489 °C indicates residual carbon or stable SnS_2 degradation. Minimal weight loss above 500 °C confirms excellent thermal stability, enhanced by strong rGO–SnS_2 interactions. The synergistic effects of rGO's framework and SnS_2's properties make the composite suitable for photocatalysis applications. The TGA results indicate a relative weight loss of 39 wt% for rGO, 47 wt% for SnS_2, and 42 wt% for RS-1. The lower weight loss observed in the RS-1 nanocomposites confirms their high purity and thermal stability.

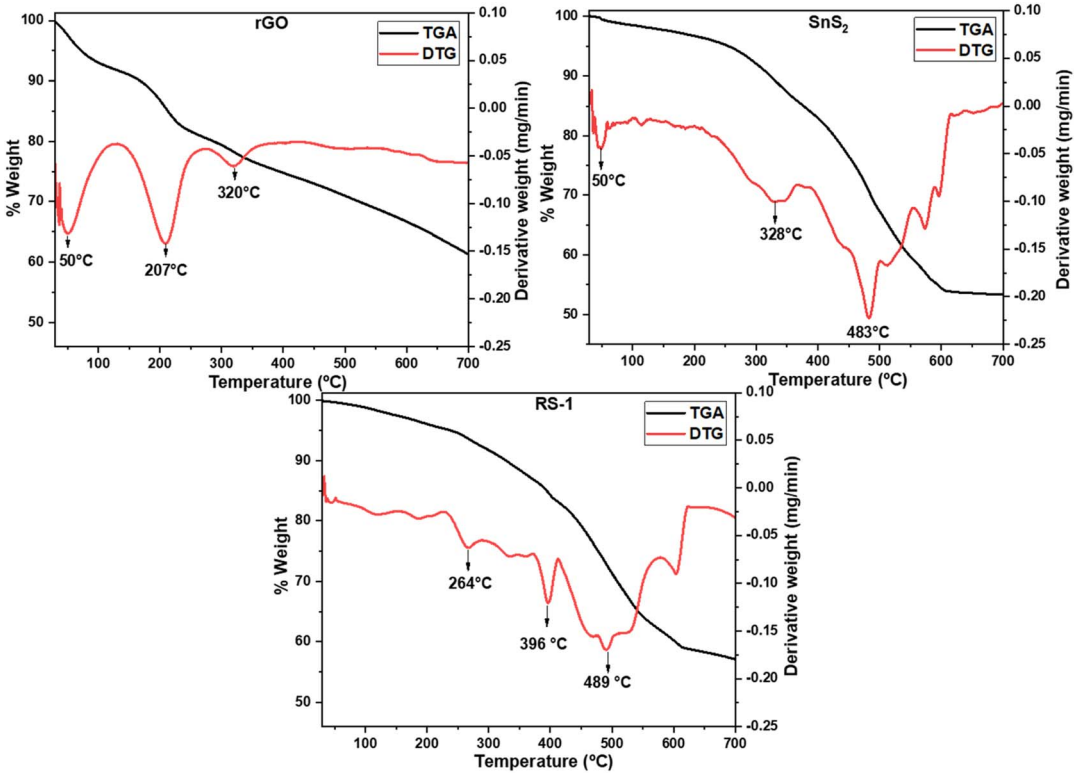

Fig. 2 TGA/DTG plots for rGO, SnS_2, and the RS-1 nanocomposite.

The TGA graph confirms that the RS nanocomposite exhibits higher thermal stability compared to SnS_2.

3.5. Optical studies

The optical properties of rGO, SnS_2, and RS nanocomposites were studied using diffuse reflectance spectroscopy. Fig. 3 shows the Tauc plot ($\alpha h\nu^2$ *vs.* $h\nu$) for rGO, SnS_2, and RS nanocomposites. The band gaps were found to be 2.61 eV for rGO and 2.43 eV for SnS_2. In the nanocomposites, no major change in the band gap of rGO was observed because it acts as the substrate material. In the RS nanocomposites, band gaps were observed for SnS_2. For the RS-0.125, RS-0.25, RS-0.5, and RS-1 nanocomposites, the band gaps of SnS_2 were estimated to be 2.3 eV, 2.26 eV, 2.19 eV, and 1.97 eV, respectively. The decrease in the band gap of SnS_2 in the RS nanocomposites from 2.3 eV to 1.97 eV indicates that the combination of carbon materials with metal sulfides reduces the band gap.[37,38]

3.6. FE-SEM analysis

Fig. 4 shows the FE-SEM images of the rGO, SnS_2, and RS nanocomposites. The inset shows the SnS_2 flakes, which are deposited over the rGO. The morphological analysis of rGO, SnS_2 nanoparticles, and RS nanocomposites was conducted using FE-SEM. The FE-SEM images of rGO reveal a flake-like morphology. For SnS_2, the images show flower-like structures surrounded by a flake-like morphology. In the RS nanocomposites, the SnS_2 nanoparticles are observed to be decorated on the rGO flakes. The FE-SEM analysis indicates that the RS nanocomposites have been successfully formed. The uniform distribution of SnS_2 nanoparticles on rGO enhances the photocatalytic activity, demonstrating improved efficiency compared to pure rGO.

3.7. TEM analysis

The morphological analysis of rGO, SnS_2 nanoparticles, and RS nanocomposites was conducted using TEM. Fig. 5 presents the TEM images, SAED patterns, and lattice fringes of rGO, SnS_2, and RS nanocomposites. The TEM images reveal that rGO exhibits a layered sheet-like morphology, while SnS_2 displays a flower-like flake morphology. The TEM image of the RS-1 nanocomposite shows SnS_2's flower-shaped flakes deposited on the surface of the rGO sheets.

The well-defined SAED pattern of rGO indicates high crystallinity (monocrystalline). The diffuse SAED pattern of SnS_2 indicates poor crystallinity, while a mixed pattern with lines and dots for RS-1 indicates polycrystalline behavior. The crystallographic lattice fringes in the TEM images show *d*-spacings of 3.57 Å and 3.31 Å in the RS-1 nanocomposite, corresponding to 2θ values of (002) for rGO. The TEM analysis confirms that the RS nanocomposite has been properly formed.

4. Photocatalytic studies of rGO and rGO–SnS_2 (RS) nanocomposites

4.1. Photocatalytic degradation and % removal studies of ATZ and 2,4-D (natural sunlight)

The degradation studies of ATZ and 2,4-D were performed using UV-Vis spectroscopy, with characteristic peaks of ATZ and 2,4-D observed at λ_{max} of 220 nm and 200 nm, respectively. Fig. 6a–d show the UV-Vis spectra and removal efficiency.

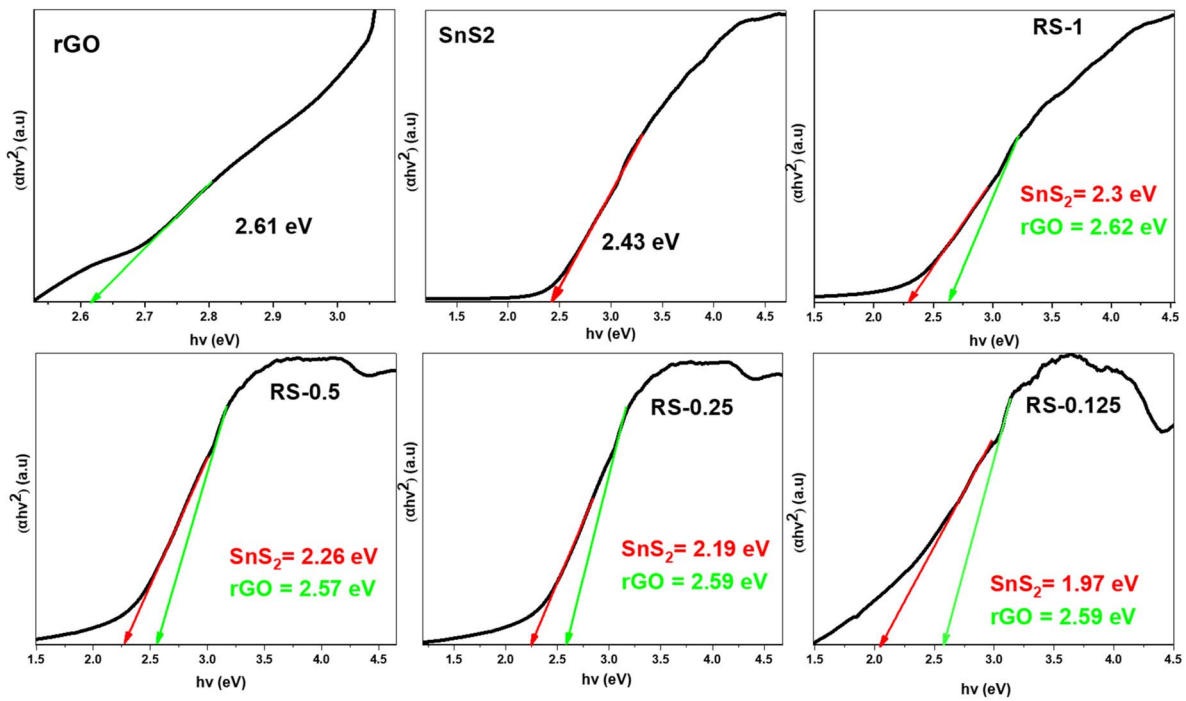

Fig. 3 $\alpha h\nu^2$ *vs.* $h\nu$ plot of rGO, SnS_2, and RS nanocomposites.

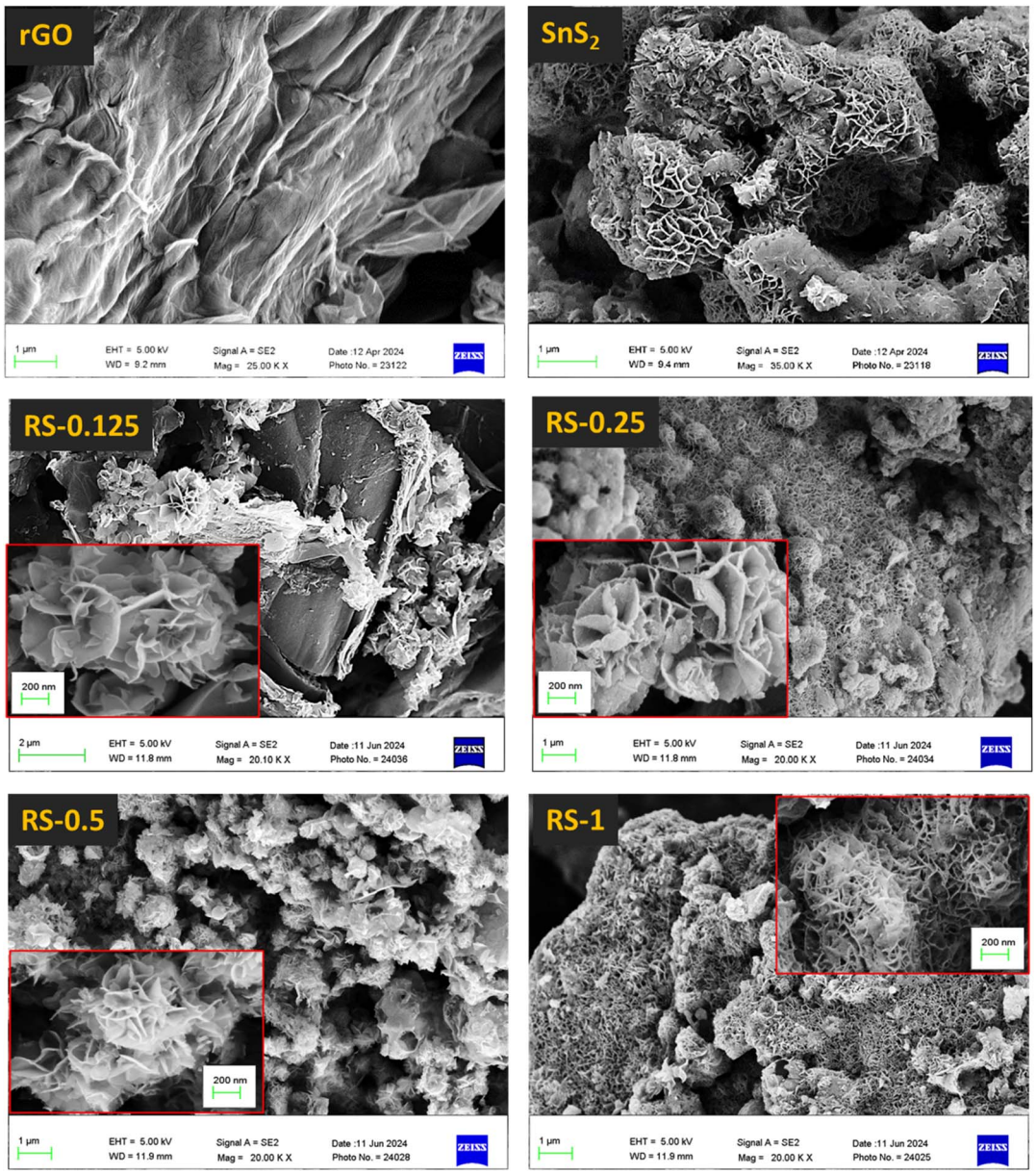

Fig. 4 FE-SEM images of rGO, SnS_2, and RS nanocomposites (insets show the zoomed-in images; scale bar of insets = 200 nm).

Fig. 6a shows the UV-Vis spectra for the degradation of ATZ using rGO and RS nanocomposites. A drastic reduction in intensity indicates the degradation of ATZ. Fig. 6c shows the % removal of ATZ using rGO and RS nanocomposites. For the degradation of ATZ, 18% removal was observed when rGO was used as a photocatalyst, after 3 minutes of irradiation. The removal studies indicate the maximum removal of 91% by the RS-1 nanocomposite in 3 minutes, followed by 33%, 61%, and 82% for RS-0.125, RS-0.25, and RS-0.5, respectively, which is higher than that of the parent compound.

Fig. 6b also shows the UV-Vis spectra for the degradation and (d) % removal of 2,4-D using rGO and RS nanocomposites. Similarly, for 2,4-D, 26% removal was observed in 3 minutes. A maximum of 87% removal was observed when the RS-1 nanocomposite was used, while other nanocomposites RS-0.125, RS-0.25, and RS-0.5 exhibit 11%, 63%, and 75% removal, respectively. The RS-1 nanocomposites demonstrate the highest removal efficiency. An enhanced degradation ability of the RS nanocomposites compared to rGO is because the incorporation of SnS_2 into the carbon matrix improves the degradation of the analyte on the surface.

Based on the graph, it is concluded that RS nanocomposites exhibit higher removal efficiency compared to rGO samples for both agrochemicals. Further testing for 15 minutes showed no additional change, confirming that 3 minutes is the optimal time for degradation (the data of kinetics and control studies have been added in ESI Fig. S2†). rGO has limitations in generating charge carriers; however, combining it with the photosensitizer material (SnS_2) enhances the removal efficiency due to the synergistic effects of the two materials. Additionally,

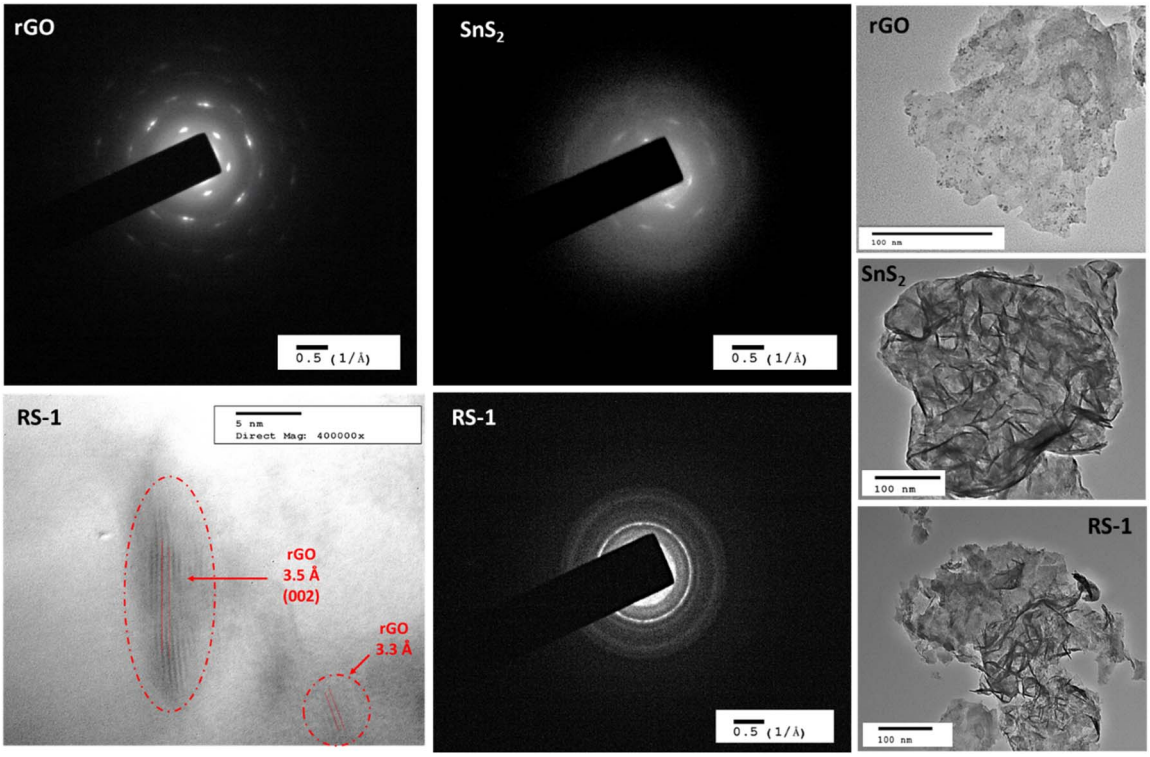

Fig. 5 TEM images and SAED pattern of rGO, SnS_2, and the RS-1 nanocomposite along with lattice fringes observed in the RS-1 nanocomposite.

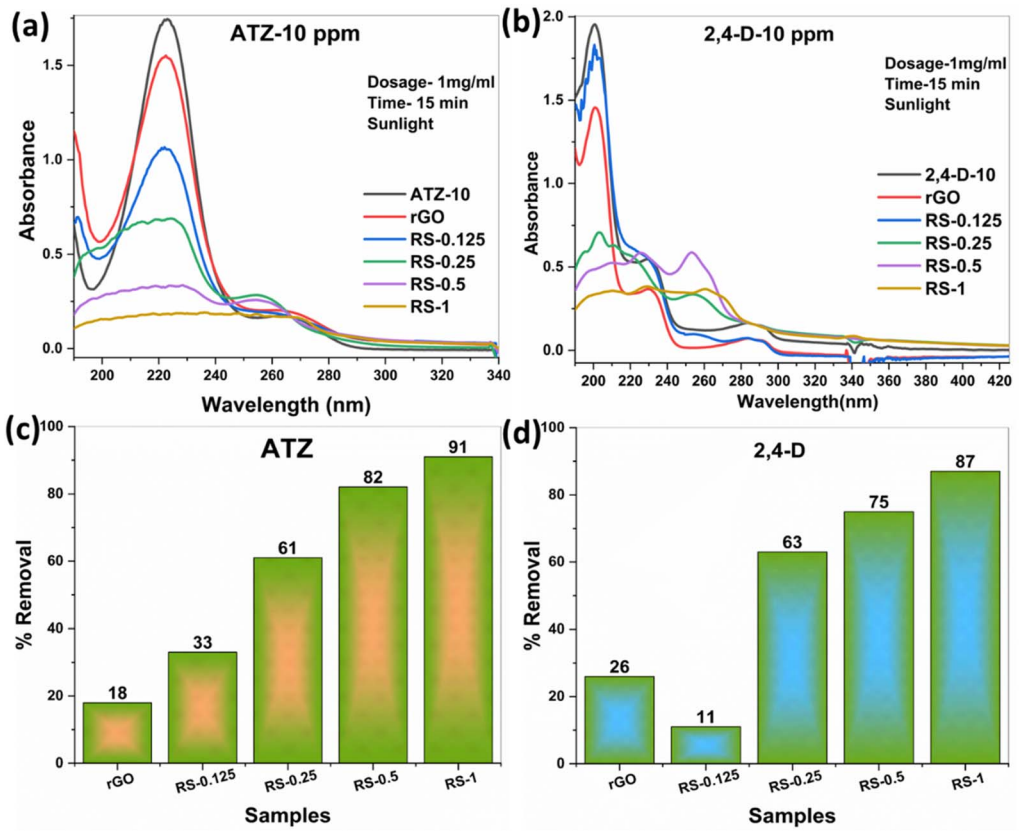

Fig. 6 UV-Vis graph showing degradation of (a) ATZ and (b) 2,4-D using rGO, RS nanocomposites, and % removal graph of (c) ATZ and (d) 2,4-D using rGO and RS nanocomposites (reaction conditions: 10 ppm solution, 1 mg ml^{-1}, 3 minutes, and sunlight).

RS nanocomposites facilitate the breakdown of ATZ and 2,4-D into major intermediates, as confirmed by UV-Vis spectroscopy and discussed in the following section 4.2.

4.2. Effect of various parameters on the photocatalyst RS-1 nanocomposite

4.2.1. Loading of SnS_2. Fig. 7a and b show the effect of SnS_2 loading in RS nanocomposites. The loading study aimed to determine how the amount of SnS_2 nanoparticles influences the photocatalytic performance of the nanocomposites. The graphs for both agrochemicals, ATZ and 2,4-D, indicate that as the loading of SnS_2 on rGO increases, the removal percentage also increases. This is because more active sites are available on the material's surface for interaction with the agrochemicals, enhancing the efficiency. However, there is a decrease in efficiency at the highest loading (RS-2). This decline is likely due to

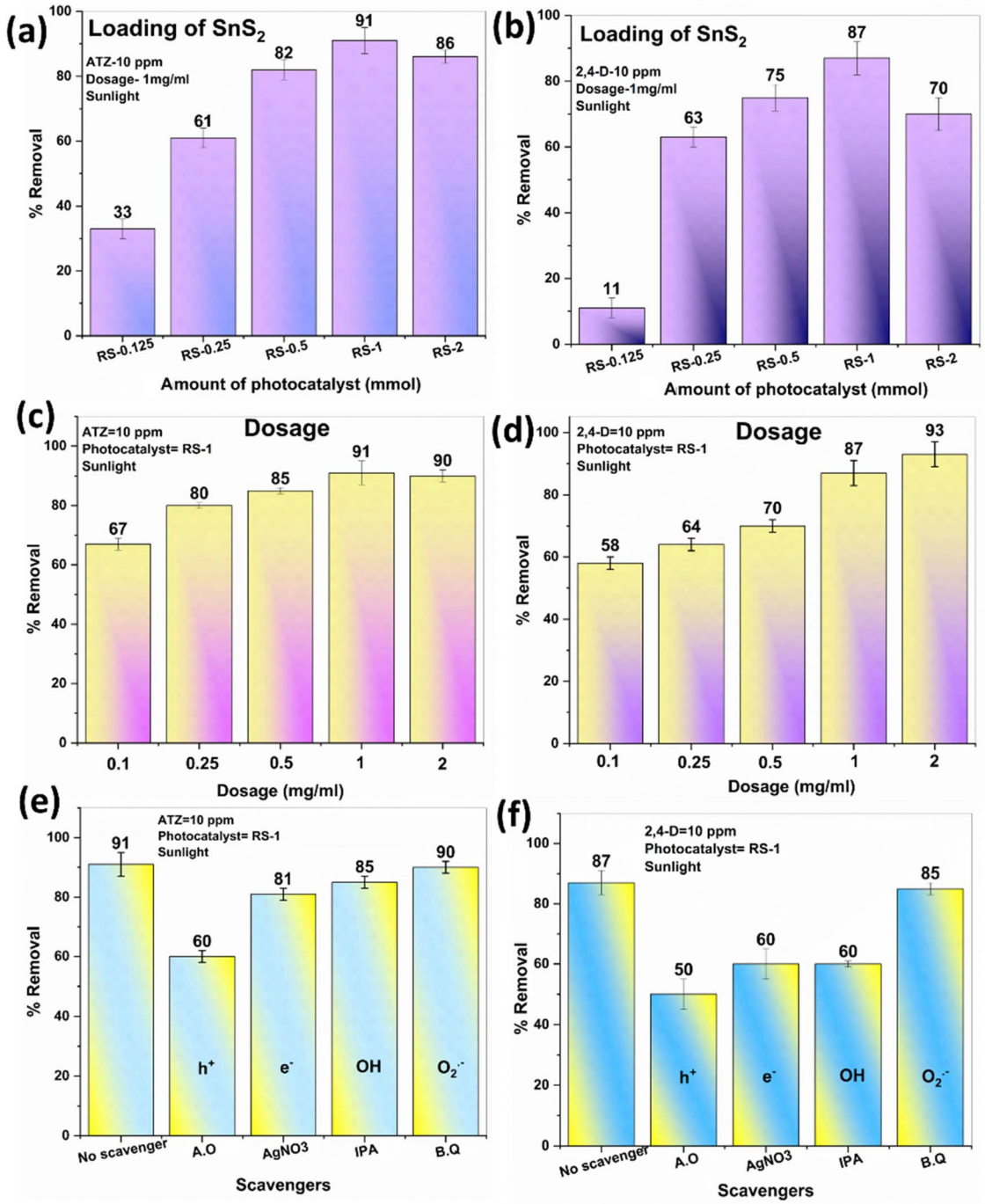

Fig. 7 Bar graph representation of % removal in ATZ (a) and 2,4-D (b) with varying amounts of SnS_2 on rGO, % removal in ATZ (c) and 2,4-D (d) with different amounts of dosage and % removal in ATZ (e) and 2,4-D (f) in the presence of different scavengers (reaction conditions: 10 ppm solution, 1 mg ml^{-1}, 3 minutes, and sunlight).

agglomeration, which reduces the surface area available for interaction with the agrochemicals, leading to lower removal efficiency.

4.2.2. Effect of catalyst dosage. A dosage study determined the optimal amount for maximum removal efficiency. Different dosages of 0.1, 0.25, 0.5, 1, and 2 mg ml^{-1} were tested for removing ATZ and 2,4-D. Fig. 7c and d illustrate the effects of dosage on the degradation of ATZ and 2,4-D using the RS-1 nanocomposite. The results show that as the dosage increased from 0.1 to 1 mg ml^{-1}, the removal percentage also increased. The maximum efficiencies observed were 91% for ATZ and 87% for 2,4-D at a dosage of 1 mg ml^{-1}. The improved performance with higher dosage is attributed to the increased availability of active sites for degradation. However, when the dosage was further increased from 1 to 2 mg ml^{-1}, there was an insignificant change in removal efficiency. Therefore, 1 mg ml^{-1} was selected as the optimal dosage for further studies.

4.2.3. Effect of pH. The pH study was conducted to determine the most suitable conditions for maximum degradation performance under different pH levels. Degradation studies were performed at various pH values ranging from 2 to 12. Fig. 8a and b show the UV spectra, while Fig. 8c and d present the percentage removal of ATZ and 2,4-D achieved in 15 minutes using the BZ-10 nanocomposite under different pH conditions.

ATZ demonstrates comparable removal efficiencies across different pH levels, with no significant changes observed, despite the structural changes at both high and low pH levels (as shown in Fig. 8a). Reports confirm that at lower pH, cyanuric acid is formed, while at higher pH, melamine is produced—both are major intermediates of ATZ.[39]

In the case of 2,4-D, a 79% removal is observed at pH 2, and as the pH increases, there is no significant change in the efficiency, with similar removal observed at higher pH levels. The UV spectrum of 2,4-D shows a shift at two wavelengths at lower pH, confirming the formation of hydroquinone (HQ), and at higher pH, the formation of hydroxycarboxylic acid (HCA).

The results from the pH studies indicate that the initial pH (ATZ = 5.7 and 2,4-D = 5.3) is more favorable for the maximum degradation of both agrochemicals. For ATZ, the RS-1 nanocomposites effectively remove cyanuric acid and melamine under acidic and basic conditions, respectively. For 2,4-D, the RS-1 nanocomposites effectively remove HQ and HCA under acidic and basic conditions, respectively. Scheme 2 illustrates the pH mechanisms for ATZ and 2,4-D degradation using rGO–SnS_2 nanocomposites under acidic and basic conditions and shows the major intermediates formed at these pH levels.

4.2.4. Stability study. The stability study examined the crystal structure stability of photocatalysts using XRD after degradation experiments. Fig. 9 shows the XRD patterns of the RS-1 nanocomposite recorded before and after the degradation experiments. The XRD patterns reveal no significant differences between the as-prepared nanocomposites and those after degradation, indicating that the structure was retained. This

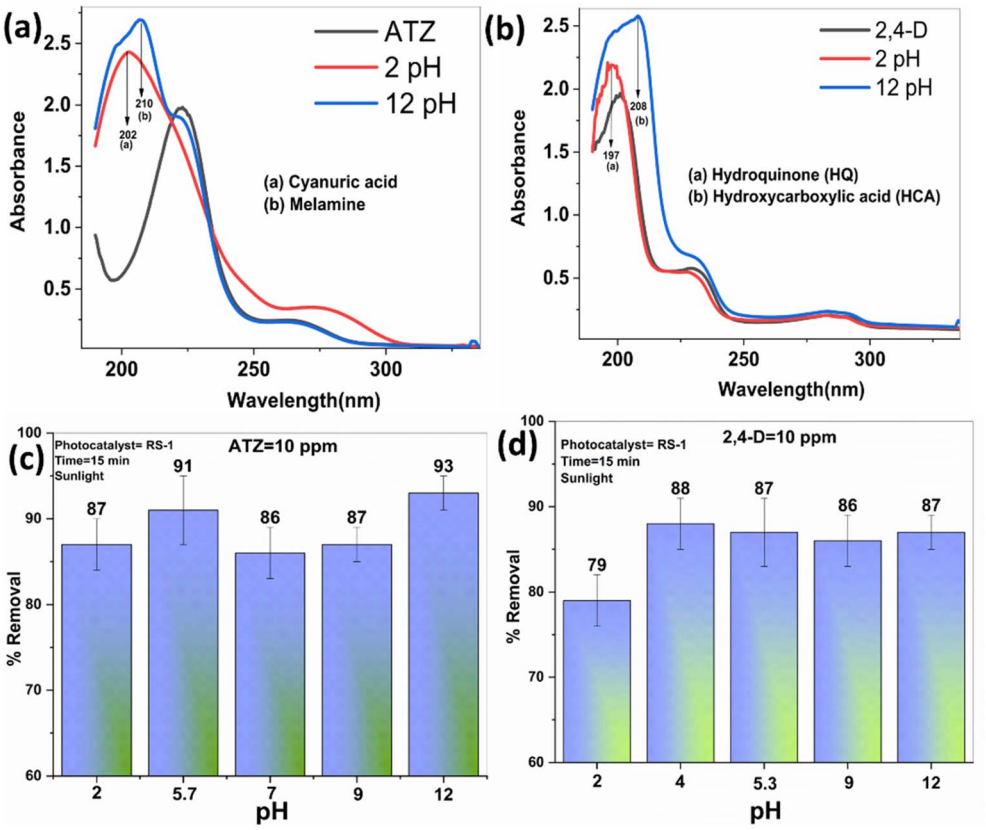

Fig. 8 UV-Vis spectra at 2 and 12 pH for ATZ (a) and 2,4-D (b), and bar graph of % removal of ATZ (c) and 2,4-D (d) at different pH levels (reaction conditions: 10 ppm solution, 1 mg ml^{-1}, 15 minutes, and sunlight).

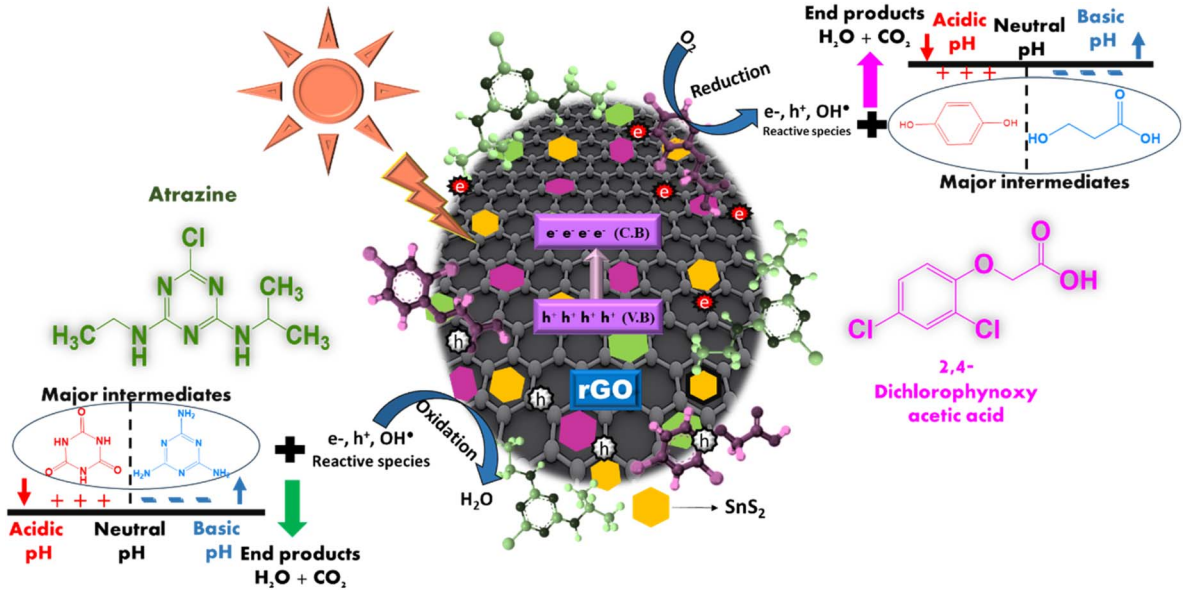

Scheme 2 Proposed schematic representation of the rGO–SnS_2 nanocomposite based on the pH studies.

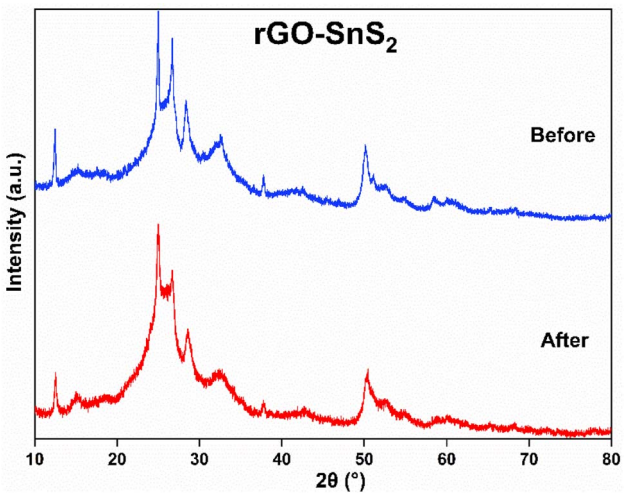

Fig. 9 Recycle study of the RS-1 nanocomposite.

demonstrates that the rGO–SnS_2 nanocomposite exhibits excellent photochemical stability.

4.3. Mechanism and degradation pathway

4.3.1. Scavenger study. Scavenger studies were conducted to identify the primary active species involved in the degradation process. Fig. 7e and f show the results of the scavenger studies for ATZ and 2,4-D using the RS-1 nanocomposite. Various scavengers, including AO, $AgNO_3$, IPA, and BQ, were used to scavenge holes, electrons, hydroxyl radicals, and superoxide radicals, respectively.

For both agrochemicals, the results concluded that holes are the primary active species involved. It was observed that scavenging hydroxyl radicals and electrons with IPA and $AgNO_3$ led to a decrease in degradation efficiency. Conversely, no significant change was observed when using BQ, suggesting that superoxide radicals do not participate in the degradation of the agrochemicals. The results indicate that holes, electrons, and hydroxyl radicals are the main active species involved in the degradation of ATZ and 2,4-D.

4.3.2. Mechanism of the Z-scheme photocatalyst for photocatalytic degradation of agrochemicals. The band structure of the rGO–SnS_2 nanocomposite suggests a possible Z-scheme photocatalytic mechanism, as proposed in Scheme 3. The enhancement in the photocatalytic activity of the rGO–SnS_2 nanocomposite is due to the synergistic effects of rGO and SnS_2, forming heterojunctions. Two possible mechanisms of heterojunctions promote the separation of charge carriers: the conventional heterojunction configuration and the direct Z-scheme configuration. The scavenger study, which showed a decrease in efficiency with the scavenging of electrons and holes, confirms that the rGO–SnS_2 system follows a Z-scheme heterojunction mechanism.[40]

In a direct Z-scheme photocatalytic system, rGO and SnS_2 absorb light due to their narrow band gaps. This light exposure excites electrons from the valence band (VB) to the conduction band (CB), leaving holes in the VB. Electrons from SnS_2's CB can then move to rGO's VB through the hetero-interface, where they recombine with holes, aiding in separating electrons from rGO's CB.[41]

rGO is an n-type semiconductor and SnS_2 is a p-type semiconductor, which together form a p–n junction in the heterojunction, a key feature for the Z-scheme. The p–n junction, which is a key feature in a typical Z-scheme heterojunction (as confirmed by the M–S analysis, described in ESI S1†), creates an internal electric field that aids in the movement of electrons toward the n-type region while holes move towards the p-type region, thereby decreasing the recombination rate of charge carriers.[40] By efficiently separating the charge carriers, the p–n

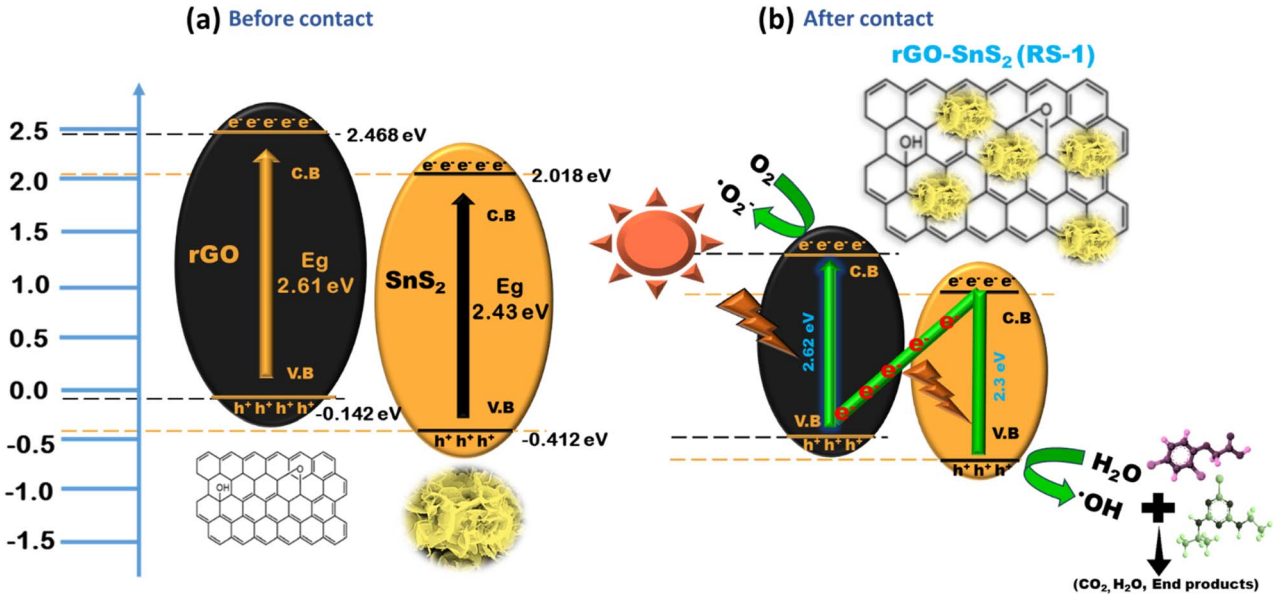

Scheme 3 Schematic representation of the conduction pathway for charge carriers in a direct Z-scheme heterojunction.

junction increases their lifetime, allowing them to participate in redox reactions on the photocatalyst surface, thereby enhancing photocatalytic activity.

The synergistic effect between rGO and SnS_2 is effective for degrading agrochemicals such as ATZ and 2,4-D. The remaining photogenerated electrons in the CB of rGO interact with oxygen molecules in the aqueous solution, producing highly active superoxide radicals ($O_2^{\bullet-}$). Simultaneously, the remaining photogenerated holes in the VB of SnS_2 interact with water or hydroxyl ions to form hydroxyl radicals. These active oxidation species (AOS), including electrons, holes, superoxide, and hydroxyl radicals, are responsible for degrading the agrochemicals. These radicals react with the agrochemicals, breaking them down into major intermediates and simpler products such as H_2O and CO_2. This process accelerates the separation of photogenerated electrons, improving the photocatalytic performance for degrading ATZ and 2,4-D agrochemicals.

Based on these findings, a possible photocatalytic degradation mechanism for these agrochemicals using rGO/SnS_2 nanocomposites is proposed.

$$(\mathrm{rGO/SnS_2})\ \text{photocatalyst} + h\nu \rightarrow e^- + h^+ \qquad \text{(a)}$$

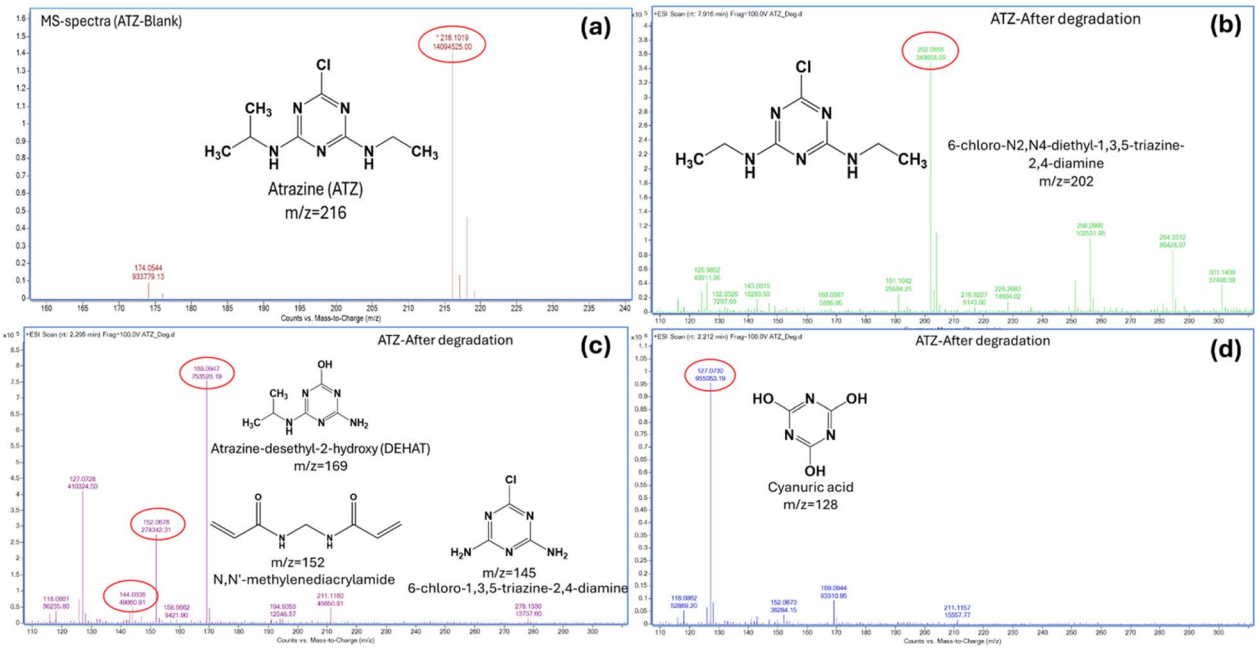

Fig. 10 Mass spectra of blank ATZ (a) and ATZ after degradation (b–d) (degraded products at different retention times).

$$e^- + O_2 \rightarrow O_2^{\bullet -} \quad (b)$$

$$h^+ + H_2O \rightarrow OH^\bullet + H^+ \quad (c)$$

$$h^+ + OH^- \rightarrow OH^\bullet \quad (d)$$

$$\text{Agro} + h\nu + \text{rGO/SnS}_2 \rightarrow \text{Agro}^{+\bullet} + \text{rGO/SnS}_2\ (e^-) \quad (e)$$

$$\text{Agro and Agro}^{+\bullet} + OH^\bullet \rightarrow \text{intermediates} + CO_2 + H_2O \quad (f)$$

4.3.3. Degradation pathway of ATZ and 2,4-D by LC-MS analysis. LC-MS techniques have been employed to investigate the degradation pathways of ATZ and 2,4-D and identify the resulting byproducts. The study observes a shift in the UV-vis absorption spectra and new peaks of the byproducts, confirming their formation (as shown in ESI S3†). This research provides a comprehensive analysis of the photocatalytic mineralization of ATZ and 2,4-D, with detailed insights into its degradation pathways based on LC-MS data. Fig. 10 and 11 show the mass spectra of a standard solution of ATZ and 2,4-D and those obtained after degradation (15 min).

The mass spectrum of ATZ shows a prominent molecular ion peak at *m*/*z* 216, which is well-documented in the literature (Fig. 10a).[3] The mass spectrum also reveals the degradation of ATZ into major metabolites with different retention times, as illustrated in Fig. 10b–d. At a retention time of 7.9 minutes, the molecular ion peak for the major metabolite, 6-chloro-*N*2, *N*4-

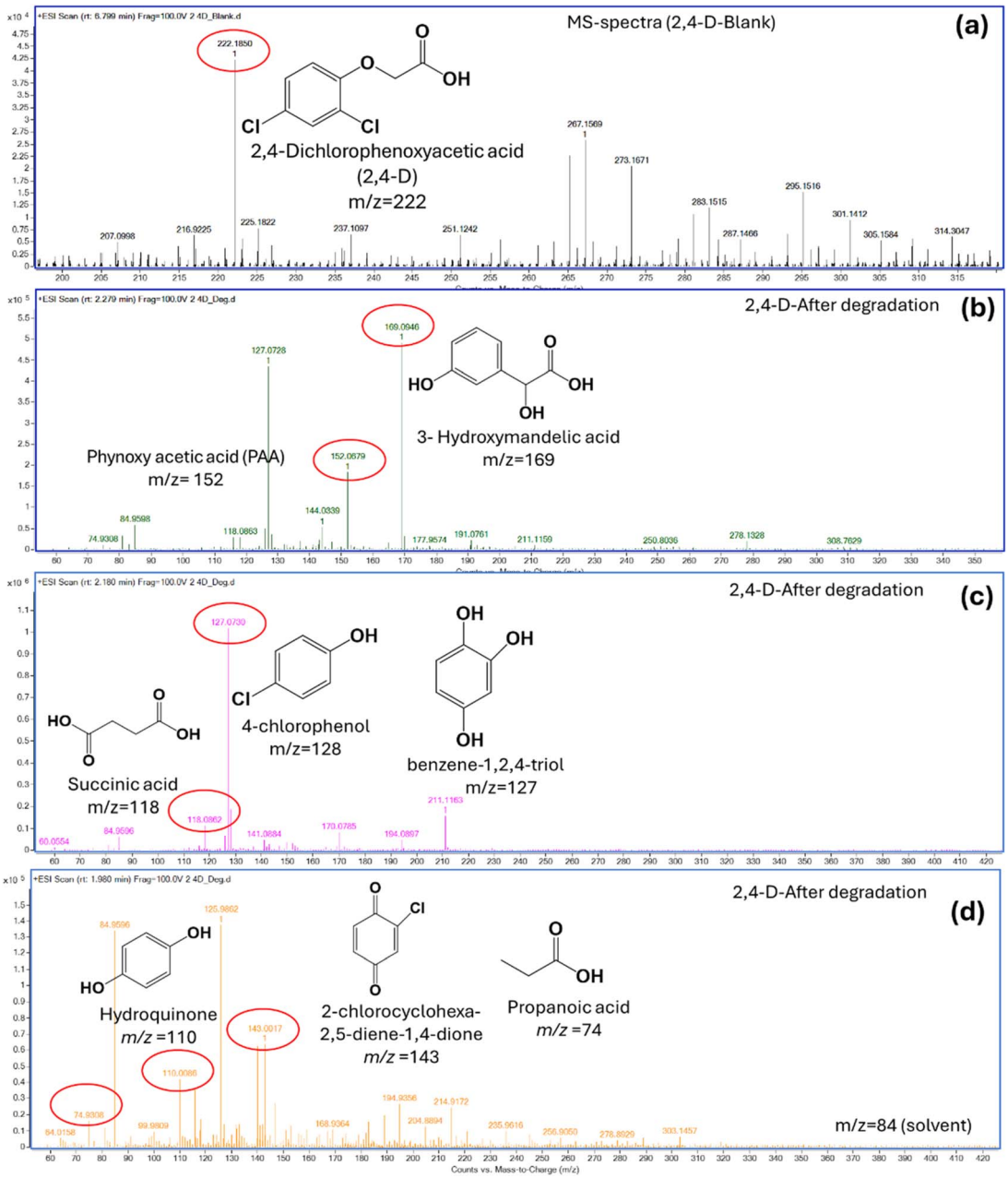

Fig. 11 Mass spectra of blank 2,4-D (a) and 2,4-D after degradation (b–d) (degraded products at different retention times).

diethyl-1,3,5-triazine-2,4-diamine, appears at *m*/*z* 202. This metabolite further degrades into 6-chloro-1,3,5-triazine-2,4-diamine, which shows a molecular ion peak at *m*/*z* 145 at a retention time of 2.29 minutes. Additionally, at the same retention time (2.29 minutes), two other metabolites, atrazine-desethyl-2-hydroxy (DEHAT) and *N*,*N*′-methylenediacrylamide, are detected with molecular ion peaks at *m*/*z* 169 and *m*/*z* 154, respectively. These metabolites are subsequently converted into ammeline or cyanuric acid at *m*/*z* 128, as seen in the mass spectra at a retention time of 2.25 minutes.

The mass spectra of 2,4-dichlorophenoxyacetic acid (2,4-D) exhibit a molecular ion peak at *m*/*z* 222, as shown in Fig. 11a.[42] Following degradation, 2,4-D is converted into various metabolites at different retention times, as shown in Fig. 11b–d. The major metabolites phenoxyacetic acid (PAA) and 3-hydroxymandelic acid are detected at *m*/*z* 152 and *m*/*z* 169, respectively, at a retention time of 2.279 minutes. These metabolites subsequently degrade into two additional products: succinic acid and benzene-1,2,4-triol or 4-chlorophenol, which are observed at *m*/*z* 118 and *m*/*z* 127, respectively, at a retention time of 2.18 minutes. Further breakdown leads to the formation of three by-products: hydroquinone, 2-chlorocyclohexa-2,5-diene-1,4-dione, and propanoic acid, which are detected at *m*/*z* 110, *m*/*z* 143, and *m*/*z* 74, respectively, at a retention time of 1.99 minutes.

Scheme 4 illustrates the breakdown of two compounds, ATZ and 2,4-D, into intermediate and final degradation products through photocatalytic degradation. These pathways involve multiple stepwise transformations leading to mineralization, highlighting the breakdown mechanisms for these compounds.

Hydroxylation, dechlorination, and de-ethylation degrade ATZ to form compounds like 6-chloro-*N*2,*N*4-diethyl-1,3,5-triazine-2,4-diamine, HAT, DEHAT, melamine, and cyanuric acid. Cyanuric acid is the terminal product in all pathways, a stable, less toxic compound indicative of complete mineralization.

The degradation of 2,4-D follows two primary pathways, leading to the breakdown of its aromatic ring and mineralization into smaller compounds. Similarly, 2,4-D breaks down into intermediates like 4-CPAA and 2,4-DCP, which are cleaved into 4-chlorophenol (4-CP) and 2-chlorophenol (2-CP). These intermediates are reduced to HQ, which undergoes further transformation to phenol and propanoic acid. These pathways highlight the stepwise cleavage of the aromatic ring, leading to the formation of simple organic compounds such as phenol, propanoic acid, and hydroxycarboxylic acid, indicating near-complete mineralization of 2,4-D. These pathways demonstrate the progressive detoxification of agrochemicals into simpler, environmentally benign molecules, as confirmed by LC-MS, UV spectroscopy, and pH studies.

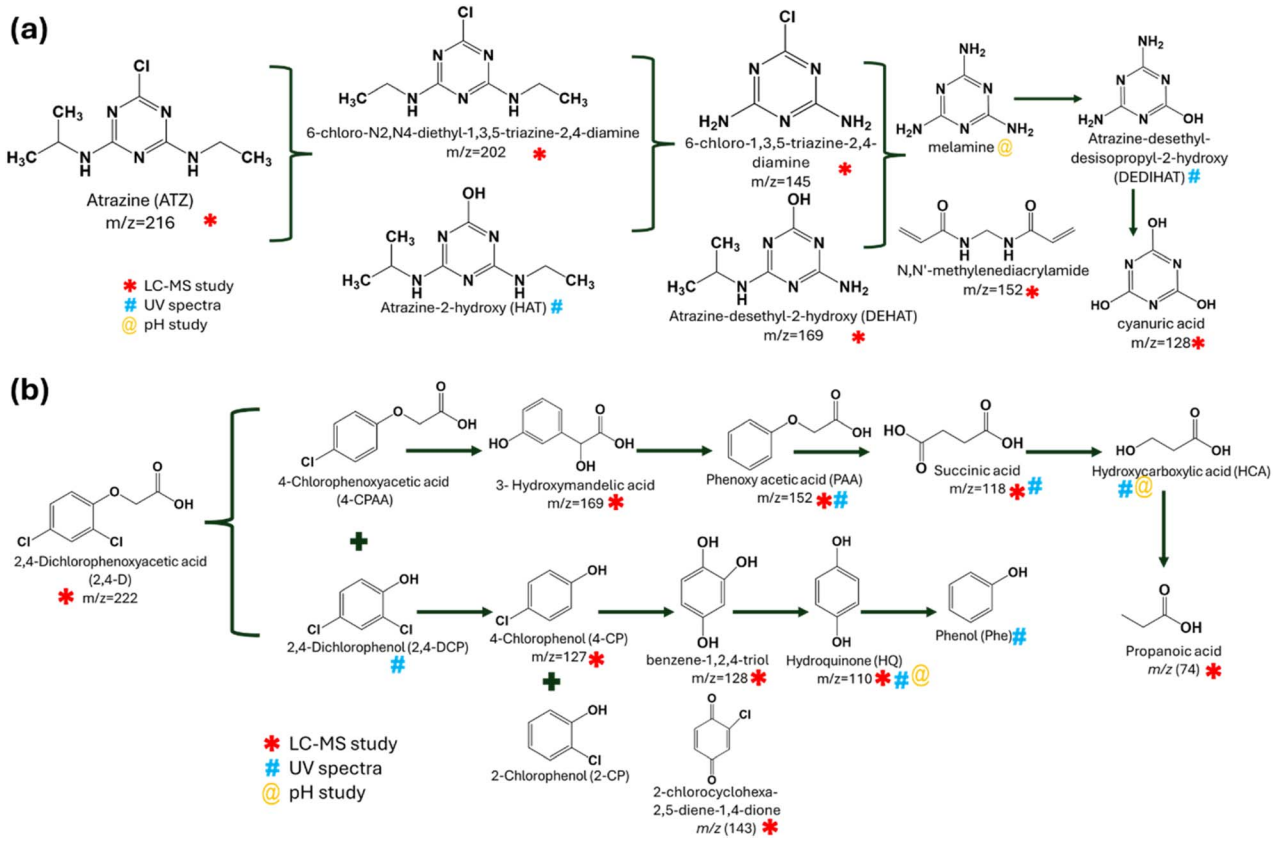

Scheme 4 Proposed degradation pathway based on the identified transformation products of (a) ATZ and (b) 2,4-D using LC-MS, pH, and UV studies.

Table 3 Summary of rGO/SnS_2 nanocomposites, conditions for different pollutants degraded using the photocatalytic process, and different photocatalysts for the degradation of ATZ and 2,4-D under different conditions

Sr. No	System	Method	Catalyst dosage	Source	Exposure time	Pollutant	Efficiency	Ref.
1	rGO/SnS_2	Hydrothermal synthesis	0.2 g L^{-1}	Visible	2.3 h	Remazol brilliant red (RBR) Remazol brilliant blue (RBB)	99% 97%	21
2	rGO/SnS_2	Hydrothermal synthesis	0.2 mg ml^{-1}	Visible	180 min	Acid orange 7	81%	43
3	rGO/SnS_2	Hydrothermal synthesis	—	Visible	90 min, 5 min, 15 min, 90 min	Nitrobenzene, methylene blue, Rhodamine B, and Cr(VI)	99.9% 99.9% 99% 94%	44
4	rGO/SnS_2/Fe_3O_4	—	—	Visible	—	Diazinon	—	45
5	rGO/SnS_2/Ag	—	—	Solar light	—	Norfloxacin	94%	46
6	rGO/SnS_2/g-C_3N_4	Hydrothermal synthesis	1 mg in 20 ml	Visible	70 min	Methylene blue	86%	47
7	MnV_2O_6/$BiVO_4$	Hydrothermal synthesis		Visible light	6 min 35 min	Methylene blue Rhodamine B	98% 96%	48
8	$Ti_{0.7}W_{0.3}O_2$/TiO_2NCl	—	0.45 g L^{-1}	UV-vis	50 min	Phenol	98.7	49
9	PAu-CQD/TiO_2		1 mg ml^{-1}	—	20 min 150 min	Methylene blue Erythromycin	—	50
10	TiO_2 P25	—	—	Sunlight	15 min	Glucocorticoids	>95%	51
11	$BiVO_4$	pH-controlled hydrothermal method	100 mg L^{-1}	200 W blue LED light	30 min	Tetracycline	96%	52
12	$BiVO_4$	—	0.6 g L^{-1}	Visible light	20 min	Ofloxacin	>90%	53
13	biochar/ZnO/g-C_3N_4	—	—	—	260 min	ATZ	85%	54
14	Graphene/g-C_3N_4	*In situ* growth method	0.3 g L^{-1}	Visible	300 min	ATZ	100%	55
15	CdS/rGO/g-C_3N_4	—	0.2 g L^{-1}	—	300 min	ATZ	90%	56
16	ZnO–g-C_3N_4/MoS_2	—	0.3 g L^{-1}	—	300 min	ATZ	80%	57
17	TiO_2	Sol–gel method	100 mg	UV light		ATZ	92%	58
18	CuO NPs	Extraction method	—	—	180 min	ATZ	57%	59
19	Mn-doped ZnO/Graphene	Solvothermal method	2 g L^{-1}	LED light	120 min	2,4-D	66%	60
20	Fe_2O_3/CeO_2/Ag	Coprecipitation method	0.02 g	UV-vis	120 min	2,4-D	75%	61
21	Fe_2O_3-doped TiO_2	Sol–gel method	—	—	—	2,4-D	48%	62
22	Ti-SBA-15/C_3N_4	—	—	Visible	180 min	2,4-D	60%	63
23	WO_3/TiO_2	*In situ* anchoring (ISA) method	—	UV-vis	270 min	2,4-D	76%	64
24	rGO/SnS_2	**Thermal decomposition**	1 mg/ml	Sunlight	3 min	ATZ	91%	This work
25	rGO/SnS_2	**Thermal decomposition**	1 mg/ml	Sunlight	3 min	2,4-D	87%	This work

The proposed degradation pathways reveal that both ATZ and 2,4-D undergo stepwise transformations involving dealkylation, hydroxylation, and aromatic ring cleavage. The identification of intermediates such as DEHAT, 4-CP, and HQ provides insights into the mechanisms underlying the breakdown processes. The formation of final products such as cyanuric acid, phenol, and propanoic acid indicates effective mineralization, which is crucial for reducing the environmental persistence and toxicity of these compounds. These findings contribute to understanding the fate of ATZ and 2,4-D in nature and provide a basis for designing effective degradation strategies.

A thorough literature review was conducted to understand the state-of-the-art application and utilization of the rGO–SnS_2 nanocomposite towards photo mineralization of agrochemicals. The existing literature indicates that to date, only six researchers have reported on the rGO–SnS_2 system in various ternary nanocomposites for the photocatalytic degradation of organic contaminants. The rGO–SnS_2 nanocomposite has been explored in limited studies; other well-established materials, such as TiO_2-based and $BiVO_4$-based photocatalysts, have been widely used for the degradation of different pollutants. Table 3 summarizes the efficiency of rGO–SnS_2 alongside other photocatalysts and other papers on the photocatalytic degradation of ATZ and 2-4-D, using a different catalyst under different reaction conditions. These studies highlight the diverse synthesis methods, operational conditions, and efficiencies achieved using various photocatalysts, including rGO–SnS_2, WO_3/TiO_2, biochar/ZnO/g-C_3N_4, TiO_2, $BiVO_4$, and their composites.

However, these synthesis methods have some disadvantages, including high temperatures, long processing times, and expensive procedures. Furthermore, an extensive literature

Table 4 Data set explanation of each investigational feature used in machine learning

Investigational features		Explanation	Feature type
Input	Photocatalyst	RS-1, RS-2, rGO, SnS_2, RS-0.125, RS-0.25, RS-0.5	Categorical
	Contaminant	Atrazine (ATZ) 2,4-Dichlorophenoxyacetic acid (2,4-D)	Categorical
	Dosage	The quantity of photocatalyst used for the experiment	Numeric
	Initial concentration of contaminant	The contaminant's initial concentration before degradation	Numeric
	Time	The total time taken by the photocatalyst for degradation	Numeric
	Volume	The total volume of the contaminant solution taken for analysis	Numeric
	pH	The pH at which degradation occurs	Numeric
Output	Removal efficiency	The percentage degradation the photocatalyst shows	Numeric

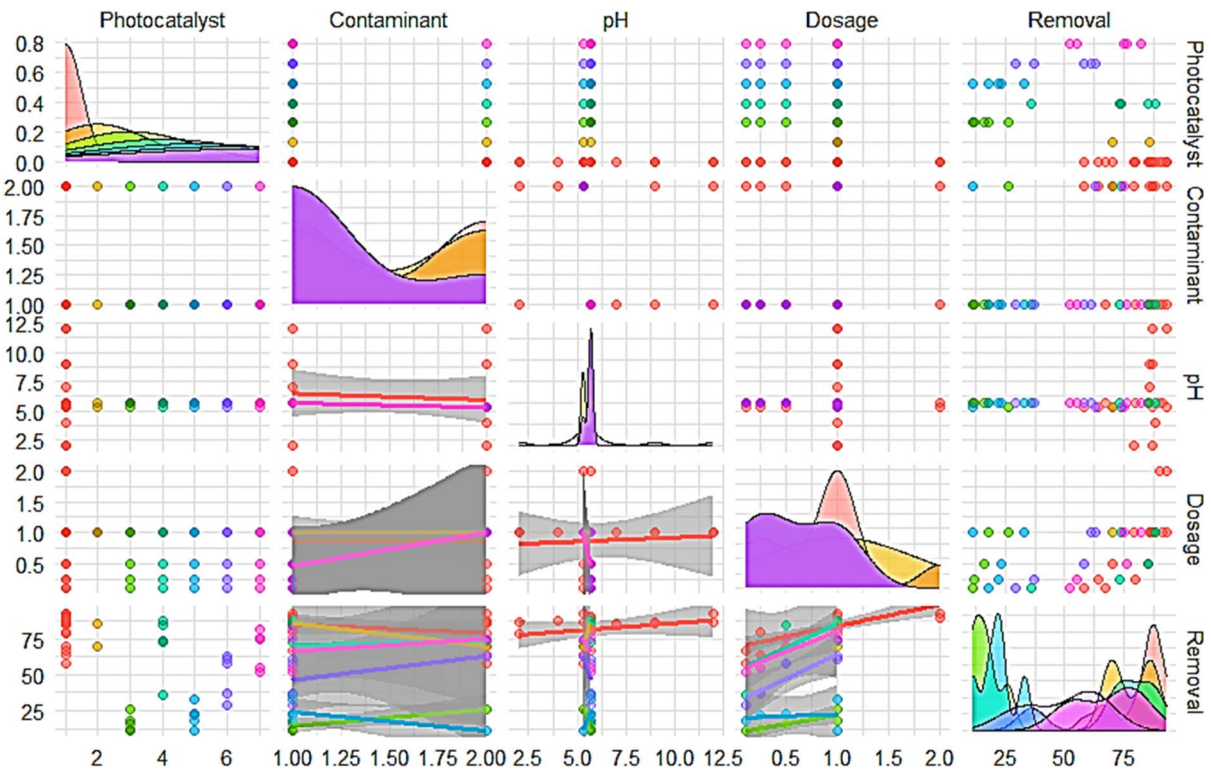

Fig. 12 Scatter matrix plot representing the distribution and trends present in the data set.

review reveals that the photocatalysts reported often have lower efficiency and require reaction times of up to 3 hours. Also, it can be noted that not many studies report the application of TiO_2-based or $BiVO_4$-based materials for the photocatalytic degradation of agrochemicals. However, these materials often require longer reaction times and specific irradiation sources, such as UV or visible light.

In contrast, the present research demonstrates the synthesis of rGO–SnS_2 nanocomposites through a single-pot, facile approach using thermal decomposition. This method is both environmentally friendly and cost-efficient. The rGO–SnS_2 nanocomposite shows superior performance, achieving 93% ATZ and 87% 2,4-D with a catalyst dosage of 1 mg per ml at pH 12 under sunlight within 3 minutes, making it a promising alternative for sustainable photocatalytic applications.

5. Predictive analysis of removal efficiency using machine learning models

Machine learning is an important aspect of artificial intelligence. Its statistical algorithms and computational power can generate a robust model capable of learning from data sets and patterns provided. These models are trained by feeding sample data, and once they learn the patterns and relationships between the variables, they can be tested on unseen and new data sets to make precise predictions. In the current study, machine learning models are only used for predictive modelling of the photocatalytic performance of the rGO–SnS_2 photocatalyst.

5.1. Data set preparation and explanation

The data obtained from experimental Section 2.6 is used for the simulation analysis of machine learning. Table 4 describes the experimental features.

5.2. Feature selection techniques

Fig. 12 depicts the scatter matrix plot showing the distribution, trends, and clusters visible in the data set. The data set is multivariate and the scatter plot helps in finding out the correlation between the variables. Photocatalysis and removal do not have any specific trend, as visible in the plot and most of the removal efficiency clusters around some specific pH values, signifying that most of the removal occurs at a specific pH. Dosage is showing a slightly upward trend with removal efficiency, indicating that increasing the dosage will increase the removal. The scatter plot only shows a visual representation, but does not quantify it. It does not provide any numerical value that quantifies the relationship between variables. To overcome these limitations, the Pearson correlation is used in a further section.

The Pearson correlation coefficient plot is used for the quantification of the relationship between variables. It gives a numeric value ranging between −1 and 1, providing a precise

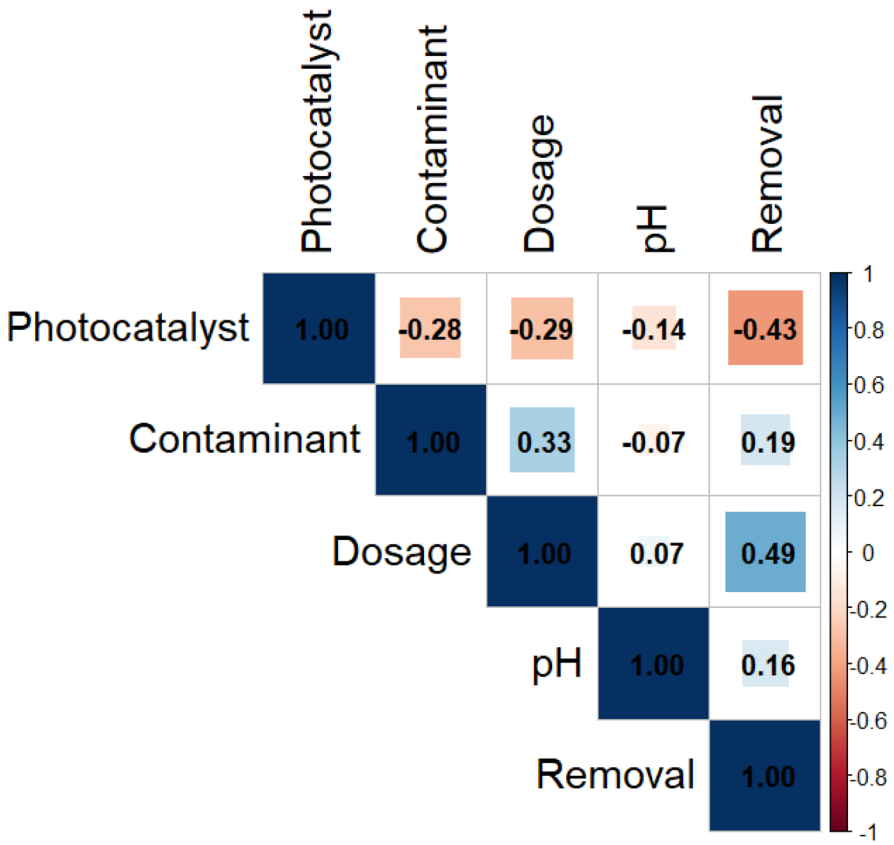

Fig. 13 Correlation coefficient plot showing the relationship between variables.

measure of the relationship between variables. Dosage and pH exhibit positive correlation values of 0.49 and 0.16, with removal efficiency, as depicted in Fig. 13. Hence, feature selection techniques identified two major variables, dosage and pH, as being strongly correlated with removal efficiency.

5.3. Application of the machine learning model for simulation

Machine learning is used for predictive analysis for the simulation of removal efficiency on the dataset obtained from the degradation results. Three modelling approaches, artificial

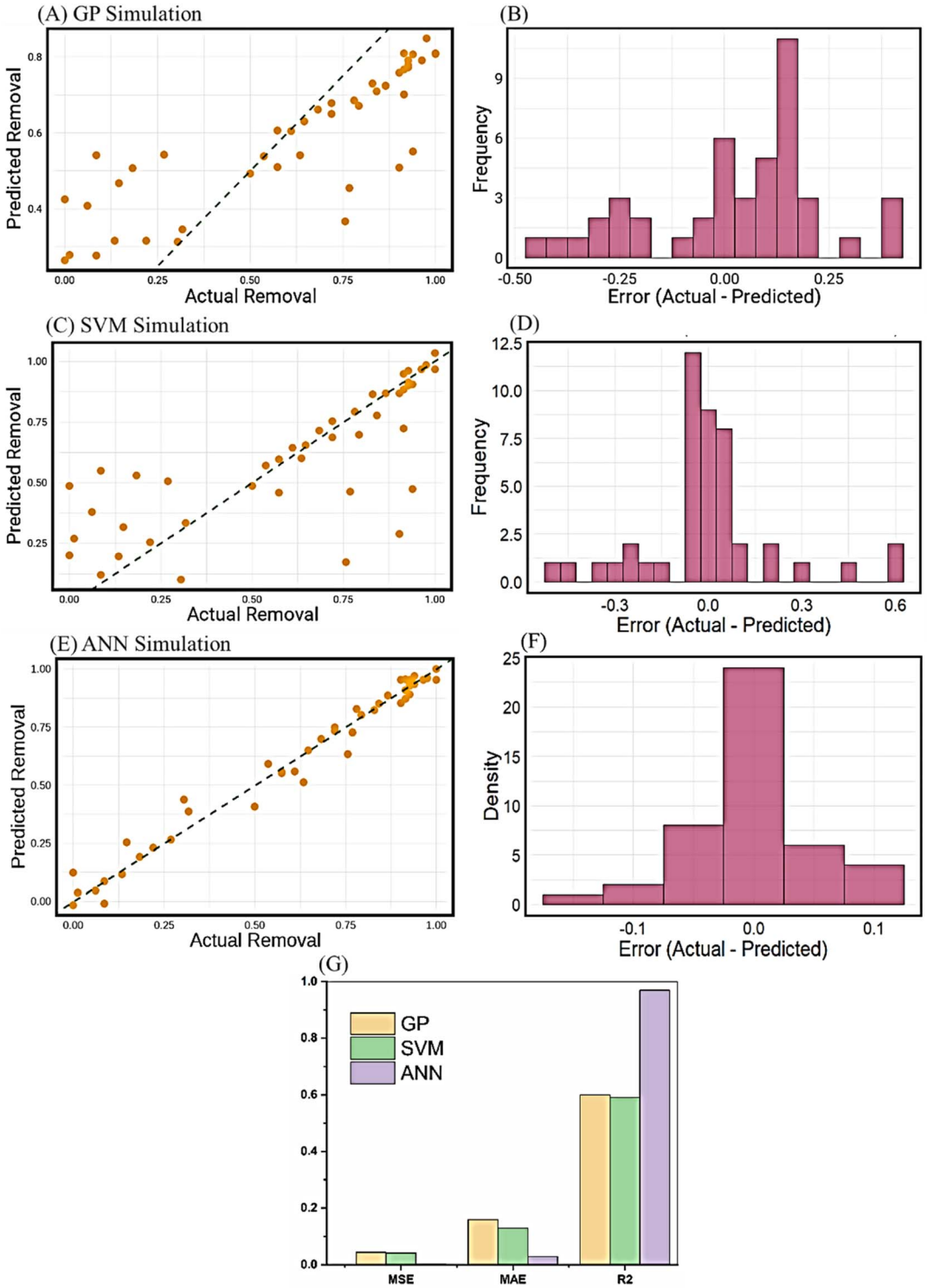

Fig. 14 (A) Plot of GP model prediction analysis, (B) residual plot of the GP model, (C) plot of SVM model prediction analysis, (D) residual plot of the SVM model, (E) plot of GP model prediction analysis, (F) residual plot of the ANN model and (G) model performance evaluation parameters.

neural network (ANN), Gaussian process (GP), and support vector machine (SVM), are fed with the data set, trained, and tested efficiently. Hyperparameters are configuration settings that need to be adjusted before feeding the model with the training set, which affect the capability of the model to learn. The number of hidden layers and neurons, step size, learning rate, activation function used, and iterations are some examples of hyperparameters for an ANN model.[65] For the SVM model, the kernel type, gamma if the radial basis function is used, and regularization parameter are some examples of hyperparameters used in the SVM model. The type of kernel, learning rate, number of iterations, and stopping criteria are some examples of the Gaussian process model. Several strategies are available for hyperparameter tuning, such as grid search, random search, Bayesian optimization, *etc.* The method used for the current models is random search, in which various combinations of hyperparameters are searched randomly. For the ANN model, the number of hidden layers is two, the number of neurons in each layer is c (7,2), the learning rate is 0.001, the logistic activation function is employed, and the maximum number of training steps is 1×10^6. The radial basis function is utilized in the SVM model, with a cost function of 10 to control the trade-off taking place between margin maximization and misclassification. For the Gaussian process model, a radial basis function kernel is used, and the model optimizes hyperparameters, including the length scale for the determination of the function's flexibility. Further information is provided in the ESI,† including hyperparameter tuning results for ANN, SVM and GP models. Mean squared error and R^2 are used as evaluation metrics for the estimation of the performance of the model.[66]

Fig. 14 depicts the simulation results of the GP, SVM, and ANN models applied. Each scatter plot describes the relationship between the actual and predicted removal efficiency for the respective models. The dashed green line represents the ideal line, and most of the data points should overlap or cluster around the ideal line, representing an accurate prediction. The R^2 values indicate the variation present between the actual and predicted removal efficiency. Fig. 14G shows the evaluation parameter values, RMSE, MAE, and R^2 of all the models applied. When comparing GP, SVM, and ANN, ANN shows accurate predictions, outperforming the other models, showcasing the lowest mean squared error and the highest R^2 values, 0.002 and 0.974, respectively. Fig. 14F shows the residual error graphs of all the models. The residual error plots of SVM and GP have a broader spread of errors, while the ANN model has most of the residual errors near zero, signifying the accurate performance and validation of the model. The symmetric distribution of errors visible in the residual plot of the ANN also implies that the model did not over-predict the removal efficiency, indicating unbiased predictions.

6. Conclusion

The present study demonstrates the successful synthesis of rGO–SnS_2 (RS) nanocomposites by a thermal decomposition approach, which were characterized by various analytical techniques confirming the proper formation of RS nanocomposites. The removal efficiencies of ATZ by rGO, RS-0.125, RS-0.25, RS-0.5, and RS-1 were 18%, 33%, 61%, 82%, and 91%, respectively. For 2,4-D, the removal efficiencies were 26%, 11%, 63%, 75%, and 87% for the same samples. The RS nanocomposites demonstrated superior removal efficiency compared to the parent compound, highlighting their enhanced photocatalytic degradation activity for agrochemicals under natural sunlight in just 3 minutes. For further studies, the optimum parameters were determined to be a concentration of agrochemicals (10 ppm), a dosage of 1 mg ml^{-1}, and pH values of 5.8 for ATZ and 7.06 for 2,4-D. Regenerability studies, confirmed by XRD analysis, showed that the photocatalyst retains excellent photochemical stability. Scavenger studies indicated that electrons, holes, and hydroxyl radicals are the main active species responsible for the degradation of ATZ and 2,4-D. Additionally, the study revealed the complete degradation of ATZ and 2,4-D into simpler products, with proposed degradation pathways supported by UV-Vis spectroscopy and LC-MS analysis. Furthermore, predictive modelling using advanced machine learning models, SVM, ANN, and GP, has been carried out for the simulation of removal efficiency. The ANN model outperformed all the other models and predicted the removal efficiency with an R^2 value of 0.99 and an error of 0.002. In summary, the rGO–SnS_2 binary heterojunction functions as a Z-scheme photocatalyst with excellent potential for wastewater treatment, and the incorporation of machine learning methodologies for predictive analysis not only validates the experimental finding but also provides a framework for optimizing and scaling the photocatalytic process.

Data availability

The authors declare that the data supporting the findings of this study are available within the paper and its ESI† files. Should any raw data files be needed in another format they are available from the corresponding author upon reasonable request.

Author contributions

Jinal Patel: formal analysis, investigation, methodology, data curation, validation, and writing – the original draft; Megha Parmar: predictive modelling analysis and writing. Syed Shahabuddin: supervision, review and editing; Inderjeet Tyagi: review and editing; Suhas: review and editing; Rama Gaur: supervision, project administration, resources, and writing – review and editing.

Conflicts of interest

The authors declare that they have no known competing financial interests or personal relationships that could have appeared to influence the work reported in this paper.

Acknowledgements

The authors would like to acknowledge the Government of Gujarat for the award of a research fellowship (KCG/SHODH/2022-23/202101585) under the Scheme for Developing High Quality Research. The authors would like to thank the Department of Chemistry, SRDC (Solar Research and Development Centre), Dr Ashish Unnarkat (Chemical Engineering Lab for TGA analysis) Gujarat Biotechnology Research Centre (LC-MS analysis), and PDEU for support in characterization and analysis facilities. The author Ms. Jinal Patel is supported by the Government of Gujarat as a Junior Research Fellow (JRF) under the Scheme of Developing High Quality Research (SHODH) (KCG/SHODH/2022-23/202101585).

References

1 J. Patel, *et al.*, A Review: Carbon-Based Materials for Photocatalytic Degradation of Agrochemicals, in *Tailored Functional Materials*, Springer Nature Singapore, Singapore, 2022.

2 D. Ahmed, *et al.*, Efficient degradation of atrazine from synthetic water through photocatalytic activity supported by titanium dioxide nanoparticles, *Z. Phys. Chem.*, 2023, **237**(4–5), 395–412.

3 L. Xu, *et al.*, Photocatalytic degradation of atrazine by H3PW12O40/Ag–TiO2: kinetics, mechanism and degradation pathways, *Chem. Eng. J.*, 2013, **232**, 174–182.

4 F. Islam, *et al.*, Potential impact of the herbicide 2,4-dichlorophenoxyacetic acid on human and ecosystems, *Environ. Int.*, 2018, **111**, 332–351.

5 G. Brucha, *et al.*, 2, 4-Dichlorophenoxyacetic acid degradation in methanogenic mixed cultures obtained from Brazilian Amazonian soil samples, *Biodegradation*, 2021, **32**, 419–433.

6 S. S, *et al.*, Photocatalytic degradation of 2,4-dichlorophenoxyacetic acid - a comparative study in hydrothermal TiO2 and commercial TiO2, *Appl. Surf. Sci.*, 2018, **449**, 371–379.

7 B. Xing, J. J. Pignatello and B. Gigliotti, Competitive Sorption between Atrazine and Other Organic Compounds in Soils and Model Sorbents, *Environ. Sci. Technol.*, 1996, **30**(8), 2432–2440.

8 S. Jha, *et al.*, Kinetic and Isothermal Investigations on the Use of Low Cost Coconut Fiber-Polyaniline Composites for the Removal of Chromium from Wastewater, *Polymers*, 2022, **14**, 4220–4264.

9 J. Patel, *et al.*, Photocatalytic mineralization of chlorpyrifos using CdS/MAX-phase nanocomposites and detailed investigation of the mechanism and degradation pathways, *New J. Chem.*, 2024, **48**(45), 19249–19265.

10 J. Patel, S. Shahabuddin and R. Gaur. Modification of Graphene as an Effective Photo-Driven Catalyst for Photo-Assisted Degradation of Chlorpyrifos, in *International Conference on Advances in Water Treatment and Management*, Springer, 2023.

11 J. Patel, *et al.*, A Facile One-Pot Approach for Synthesis of Graphene-CdS Nanocomposites and Implementation towards Visible Light Driven Photocatalytic Degradation of Chlorpyrifos (One-Pot Synthesis of G-CdS for the degradation of CPY), *ChemistrySelect*, 2024, **9**(2), e202302762.

12 J. Patel, *et al.*, Predictive Modeling and Analysis of Photocatalytic Degradation Performance of Biochar-ZnO Nanocomposites on Different Agrochemicals, *Int. J. Environ. Res.*, 2025, **19**(3), 66.

13 H. Raol, *et al.*, Development of MAX-Phase/CdS hybrid nanocomposite as an efficient photocatalyst for industrial wastewater treatment, *Mater. Sci. Technol.*, 2024, 02670836251323812.

14 B. Agrawal, *et al.*, Efficient synthesis of a new heterogeneous gold nanocatalyst stabilized by di-alkyne ligand and its applications for photocatalytic dye degradation and transfer hydrogenation reaction, *J. Nanopart. Res.*, 2021, **23**, 1–12.

15 A. T. Smith, *et al.*, Synthesis, properties, and applications of graphene oxide/reduced graphene oxide and their nanocomposites, *Nano Mater. Sci.*, 2019, **1**(1), 31–47.

16 L. Paramanik, K. H. Reddy and K. M. Parida, An energy band compactable B-rGO/PbTiO3 p–n junction: a highly dynamic and durable photocatalyst for enhanced photocatalytic H2 evolution, *Nanoscale*, 2019, **11**(46), 22328–22342.

17 A. Sarkar, *et al.*, High-Performance rGO-ZnO/WO3 heterojunction photocatalyst for solar green hydrogen generation, *J. Chem. Sci.*, 2023, **136**(1), 2.

18 X. Hu, *et al.*, Heterojunction Cu2O/RGO/BiVO4 ternary nanocomposites with enhanced photocatalytic activities towards degradation of rhodamine B and tetracycline hydrochloride, *New J. Chem.*, 2019, **43**(46), 18240–18250.

19 R. M. A. Iqbal, *et al.*, Development of Ag(0.04)ZrO(2)/rGO heterojunction, as an efficient visible light photocatalyst for degradation of methyl orange, *Sci. Rep.*, 2022, **12**(1), 12308.

20 D. Sharma, *et al.*, Structural, optical and photoelectrochemical properties of phase pure SnS and SnS2 thin films prepared by vacuum evaporation method, *J. Alloys Compd.*, 2020, **822**, 153653.

21 L. Dashairya, *et al.*, *SnS2/RGO Based Nanocomposite for Efficient Photocatalytic Degradation of Toxic Industrial Dyes under Visible-Light Irradiation*, 2019, vol. 774, pp. 625–636.

22 L. Dashairya, *et al.*, SnS2/RGO based nanocomposite for efficient photocatalytic degradation of toxic industrial dyes under visible-light irradiation, *J. Alloys Compd.*, 2019, **774**, 625–636.

23 M. Pirsaheb, *et al.*, Persulfate activation by magnetic SnS2-Fe3O4/rGO nanocomposite under visible light for detoxification of organophosphorus pesticide, *J. Mol. Liq.*, 2022, **364**, 119975.

24 M. Zhang, *et al.*, Highly oriented SnS2/RGO/Ag heterostructures for boosting photoeletrochemical and photocatalytic performances via schottky and RGO-n dual-heterojunctions interfacial effects, *Appl. Catal., A*, 2018, **563**, 118–126.

25 S. C. Shyagathur, *et al.*, SnS2 based SnS2/rGO/g-C3N4 Z-scheme ternary nanocomposites for efficient visible light-driven photocatalytic activity, *Opt. Mater.*, 2024, **147**, 114688.
26 M. Parmar, *et al.*, Synthesis of eco-friendly polyaniline-zeolite nanocomposite for pollutant remediation: empowered by robust machine learning algorithm, *J. Clean. Prod.*, 2024, **470**, 143339.
27 I. Melendez-Pastor, *et al.*, Environmental factors influencing DDT–DDE spatial distribution in an agricultural drainage system determined by using machine learning techniques, *Environ. Geochem. Health*, 2023, **45**(12), 9067–9085.
28 Z. H. Jaffari, *et al.*, Machine learning approaches to predict the photocatalytic performance of bismuth ferrite-based materials in the removal of malachite green, *J. Hazard Mater.*, 2023, **442**, 130031.
29 M. R. Karim and S. Hayami, Chemical, thermal, and light-driven reduction of graphene oxide: approach to obtain graphene and its functional hybrids, *Graphene materials—Advanced applications*, 2017, p. 89.
30 A. T. Habte and D. W. Ayele, Synthesis and characterization of reduced graphene oxide (rGO) started from graphene oxide (GO) using the tour method with different parameters, *Adv. Mater. Sci. Eng.*, 2019, **2019**(1), 5058163.
31 R. Gaur and P. Jeevanandam, Synthesis of SnS2 nanoparticles and their application as photocatalysts for the reduction of Cr (VI), *J. Nanosci. Nanotechnol.*, 2018, **18**(1), 165–177.
32 A. Kumar, A. M. Sadanandhan and S. L. Jain, Silver doped reduced graphene oxide as a promising plasmonic photocatalyst for oxidative coupling of benzylamines under visible light irradiation, *New J. Chem.*, 2019, **43**(23), 9116–9122.
33 R. Lather and P. Jeevanandam, Synthesis of Zn2+ doped SnS2 nanoparticles using a novel thermal decomposition approach and their application as adsorbent, *J. Alloys Compd.*, 2022, **891**, 161989.
34 G. B. Mahendran, *et al.*, Green preparation of reduced graphene oxide by Bougainvillea glabra flower extract and sensing application, *J. Mater. Sci.: Mater. Electron.*, 2020, **31**, 14345–14356.
35 F. T. Johra, J.-W. Lee and W.-G. Jung, Facile and safe graphene preparation on solution based platform, *J. Ind. Eng. Chem.*, 2014, **20**(5), 2883–2887.
36 U.-a. Kanta, *et al.*, Preparations, characterizations, and a comparative study on photovoltaic performance of two different types of graphene/TiO2 nanocomposites photoelectrodes, *J. Nanomater.*, 2017, **2017**(1), 2758294.
37 P. Gholami, *et al.*, Sonocatalytic activity of biochar-supported ZnO nanorods in degradation of gemifloxacin: synergy study, effect of parameters and phytotoxicity evaluation, *Ultrason. Sonochem.*, 2019, **55**, 44–56.
38 H. Li, *et al.*, An investigation of the biochar-based visible-light photocatalyst via a self-assembly strategy, *J. Environ. Manag.*, 2018, **217**, 175–182.
39 M. H. Almatarneh, A. A. Abu-Saleh and I. A. Elayan, Mechanistic and spectral investigation on the deamination of ammeline and ammelide, *Comput. Theor. Chem.*, 2017, **1117**, 92–99.
40 R. Ye, *et al.*, Fabrication of CoTiO3/g-C3N4 hybrid photocatalysts with enhanced H2 evolution: Z-scheme photocatalytic mechanism insight, *ACS Appl. Mater. Interfaces*, 2016, **8**(22), 13879–13889.
41 J. Low, J. Yu and C. Jiang, Design and fabrication of direct Z-scheme photocatalysts, in *Interface Science and Technology*, Elsevier, 2020, pp. 193–229.
42 N. Orooji, *et al.*, Photocatalytic degradation of 2, 4-dichlorophenoxyacetic acid using Fe3O4@ TiO2/Cu2O magnetic nanocomposite stabilized on granular activated carbon from aqueous solution, *Res. Chem. Intermed.*, 2020, **46**(5), 2833–2857.
43 A. Rahimi, I. Kazeminezhad and S. E. Mousavi Ghahfarokhi, Synthesis and investigation of SnS2/RGO nanocomposites with different GO concentrations: structure and optical properties, photocatalytic performance, *J. Mater. Sci.: Mater. Electron.*, 2018, **29**, 4449–4456.
44 H. Chauhan, Tandem photocatalysis of graphene-stacked SnS2 nanodiscs and nanosheets with efficient carrier separation, *ACS Omega*, 2016, **1**(1), 127–137.
45 M. Pirsaheb, *et al.*, *Persulfate Activation by Magnetic SnS2-Fe3O4/rGO Nanocomposite under Visible Light for Detoxification of Organophosphorus Pesticide*, 2022, vol. 364, p. 119975.
46 M. Zhang, *et al.*, *Highly Oriented SnS2/RGO/Ag Heterostructures for Boosting Photoeletrochemical and Photocatalytic Performances via Schottky and RGO-N Dual-Heterojunctions Interfacial Effects*, 2018, vol. 563, pp. 118–126.
47 S. C. Shyagathur, *et al.*, *SnS2 based SnS2/rGO/g-C3N4 Z-scheme ternary nanocomposites for efficient visible light-driven photocatalytic activity*, 2024, vol. 147, p. 114688.
48 K. Bano, *et al.*, Sunlight driven photocatalytic degradation of organic pollutants using a MnV2O6/BiVO4 heterojunction: mechanistic perception and degradation pathways, *Nanoscale Adv.*, 2021, **3**(22), 6446–6458.
49 Z. Dong, *et al.*, Preparation of a Ti0.7W0.3O2/TiO2 nanocomposite interfacial photocatalyst and its photocatalytic degradation of phenol pollutants in wastewater, *Nanoscale Adv.*, 2020, **2**(1), 425–437.
50 A. Thakur, *et al.*, TiO2 nanofibres decorated with green-synthesized PAu/Ag@CQDs for the efficient photocatalytic degradation of organic dyes and pharmaceutical drugs, *RSC Adv.*, 2020, **10**(15), 8941–8948.
51 L. Pretali, *et al.*, TiO2-Photocatalyzed Water Depollution, a Strong, yet Selective Depollution Method: New Evidence from the Solar Light Induced Degradation of Glucocorticoids in Freshwaters, *Appl. Sci.*, 2021, **11**, 1–13.
52 M. Obaid Qamar, K. Balu and Y.-H. Ahn, BiVO4-Driven photocatalytic degradation of pharmaceutical in Slurry Bubble Column Reactor: influencing factors and toxicological profiling, *Chem. Eng. J.*, 2024, **496**, 153526.
53 Y. Wen, *et al.*, S-scheme BiVO4/CQDs/β-FeOOH photocatalyst for efficient degradation of ofloxacin: reactive oxygen species transformation mechanism insight, *Chemosphere*, 2022, **295**, 133784.

54 X. An, Core-shell P-laden biochar/ZnO/g-C3N4 composite for enhanced photocatalytic degradation of atrazine and improved P slow-release performance, *J. Colloid Interface Sci.*, 2022, **608**, 2539–2548.
55 K. Altendji and S. J. C. Hamoudi, Efficient photocatalytic degradation of aqueous atrazine over graphene-promoted g-C3N4 nanosheets, *Catalysts*, 2023, **13**(9), 1265.
56 J. W. Jo WanKuen and N. Selvam, Z-scheme CdS/g-C3N4 composites with RGO as an electron mediator for efficient photocatalytic H2 production and pollutant degradation, *Chem. Eng. J.*, 2017, **317**, 913–924.
57 W.-K. Jo, J. Y. Lee and N. C. S. Selvam, Synthesis of MoS2 Nanosheets Loaded ZnO–G-C3n4 Nanocomposites for Enhanced Photocatalytic Applications, *Chem. Eng. J.*, 2016, **289**, 306–318.
58 D. Ahmed, Efficient degradation of atrazine from synthetic water through photocatalytic activity supported by titanium dioxide nanoparticles, *Zeitschrift für Physikalische Chemie*, 2023, **237**(4–5), 395–412.
59 H. Arif, Photocatalytic degradation of atrazine and abamectin using Chenopodium album leaves extract mediated copper oxide nanoparticles, *Zeitschrift Für Physikalische Chemie*, 2023, **237**(6), 689–705.
60 R. Ebrahimi, Photocatalytic Degradation of 2, 4-dichlorophenoxyacetic Acid in Aqueous Solution Using Mn-Doped ZnO/graphene Nanocomposite under LED Radiation, *J. Inorg. Organomet. Polym. Mater.*, 2020, **30**, 923–934.
61 Z. Karimipour, Photocatalytic Degradation of 2, 4-Dichlorophenoxyacetic Acid Using Fe2O2/CeO2/Ag Composite Nanoparticles under Ultraviolet, *J. Adv. Environ. Health Res.*, 2021, **9**(3), 191–200.
62 A. Razani, Sol-gel synthesis of Fe2O3-doped TiO2 photocatalyst for optimized photocatalytic degradation of 2, 4-dichlorophenoxyacetic acid, *Orient. J. Chem.*, 2017, **33**(4), 1959.
63 H. T. Duong, Photocatalytic Activity of Ti-SBA-15/C3N4 for Degradation of 2, 4-Dichlorophenoxyacetic Acid in Water under Visible Light, *J. Anal. Methods Chem.*, 2022, **2022**(1), 5531219.
64 L. M. Carvalho, 2, 4-Dichlorophenoxyacetic acid (2, 4-D) photodegradation on WO 3-TiO 2-SBA-15 nanostructured composite, *Environ. Sci. Pollut. Res.*, 2021, **28**, 7774–7785.
65 R. Abdarnezhadi and A. Mehrizad, Flowerlike Sm–ZnIn2S4 as a Susceptible Visible-Light Photocatalyst for Cr6+ Reduction: Experimental Design, RSM, and ANN Modeling, *J. Inorg. Organomet. Polym. Mater.*, 2023, **33**(6), 1621–1637.
66 N. Bagherlou, *et al.*, Optimization and modeling of betamethasone removal from aqueous solutions using a SiO2/g-C3N5@NiFe2O4 nanophotocatalyst by RSM, *npj Clean Water*, 2024, **7**(1), 2.